https://doi.org/10.1016/j.ijrmms.2021.104702

An Experimental and Analytical Study of Rate-Dependent Shear Behaviour of Rough Joints

Li, Hua (Li H.)[1], Deng, Jianhui (Deng J.H.)[1], Yin, Jianhua (Yin J.H.)[2], Qi, Shengwen (Qi S.W.), Zheng[3], Bowen (Zheng B.W.)[3], Zhu, Jianbo (Zhu J.B.)[4,5,*]

[1] State Key Laboratory of Hydraulics and Mountain River Engineering, Sichuan University, Chengdu, China

[2] Department of Civil and Environmental Engineering, The Hong Kong Polytechnic University, Hong Kong, China

[3] Institute of Geology and Geophysics, Chinese Academy of Sciences, Beijing, China

[4] Guangdong Provincial Key Laboratory of Deep Earth Sciences and Geothermal Energy Exploitation and Utilization, Institute of Deep Earth Sciences and Green Energy, College of Civil and Transportation Engineering, Shenzhen University, Shenzhen, China

[5] Shenzhen Key Laboratory of Deep Underground Engineering Sciences and Green Energy, Shenzhen University, Shenzhen, 518060, China

* Corresponding author; Email: jbzhu@tju.edu.cn

Abstract:

Understanding the shear behaviour of rough joints is of great significance for dealing with rock engineering problems. In many cases, rock joints are often subjected to dynamic loadings, which are usually caused by explosions, impacts or earthquakes, etc. Until now, the dynamic shear characteristics of rock joints have not been well understood. In the present study, we investigate joint shear behaviour at different shear rates and develop a rate-dependent constitutive model of rough joints. Testing results shows that the shear/frictional strength of joints with meso-roughness (i.e., planar joints) is independent on the shear rate, while the strength of joints with macro-unevenness (i.e., saw-toothed joints) increases with the shear rate. Under identical boundary conditions, the residual strength of joints with macro-unevenness approximates to the kinetic frictional strength of planar joints. Based on the testing results, the shear stress-displacement curve of rough joints was divided into four phases, i.e., linear elastic phase, shear hardening phase, shear softening phase and residual strength phase. A viscous joint model was thus proposed and validated through comparison with laboratory measurements. This new model correlates the static joint shear stiffness with dynamic one, and has the ability to describe the shear stiffness evolution during the whole shearing process. Based on the proposed model, a hypothesis about shear rate effects of rough joints was introduced and then verified through numerical modelling. The findings in this paper could facilitate better understanding the dynamic behaviour of rough joints and be useful for analyzing rock engineering problems with discontinuous rock masses.

Keywords: rock joint; direct shear; rate effect

1 Introduction

The analysis of rock slopes, foundations and underground openings is strongly dependent on reliable estimations of joint shear properties. To date, the shear behaviour of joints under static or quasi-static loading conditions has been extensively studied [1-3], where strain rates were usually lower than 10^{-2} s^{-1}. Besides static loads, rock masses are often subjected to dynamic loads from blasts, impacts or earthquakes, etc. The strain rate is higher than 10^{-2} s^{-1}, and the rate-dependent shear behaviour of joints is significant [4]. This shear-rate dependency was first identified by Green and Perkins [5], who suggested that the rate-dependent behaviour of rock should be considered when strain rate reaches 10^{-1} s^{-1}. Therefore, it is of high academic interests and engineering importance to understand the rate-dependent behaviour of rock joints, which are usually rough.

Although joint shear properties are influenced by the type of joints, two general agreements on shear rate effects have been reached. First, shear strength rises with the increasing shear rate. Second, the rate-dependent shear behaviour of joints is independent of normal stresses under dynamic conditions [6-8]. Recently, a number of dynamic shear systems have been developed [9, 10]. Laboratory tests on rock joints were conducted under new testing conditions. Mirzaghorbanali *et al.* [11] investigated shear rate effects under cyclic loadings and found that the dynamic frictional strength at high shear rates is increasingly higher than that at low shear rates with the rise of the number of loading cycles. Atapour and Moosavi [12] studied the dynamic shear behaviour of rough joints under constant normal stiffness conditions. They found that the shear mechanism may change from frictional sliding to asperities' breaking with increasing shear velocity. However, the joint shear behaviour under dynamic loadings is still poorly understood. Most efforts were paid to the peak strength and frictional angle. The influence of shear rates on shear displacement, joint roughness and residual strength was ignored.

Previous studies have suggested that the difference between dynamic and static joint shear behaviour could be explained by shear rate effects [6, 13-15], whereas there is still a lack of knowledge on its mechanism. One possible explanation is based on the hydromechanics and named "Stefan effect" [16], which indicates that the tensile stress applied perpendicular to the plane of microcracks is in direct proportion to the opening velocity and the viscosity of the filled liquid [16, 17]. Thus, a higher loading/strain rate would induce a higher cohesive force between crack surfaces. Another explanation is related to the inertia. At the micro scale, the inertia effect is reckoned as the increased resistance at crack tips to any sudden changes in position and state of motion [18]. This

force increment is usually expressed as a function of particle acceleration [19, 20]. At the macro scale, the increase of joint shear resistance is attributed to the confinement from surrounding rock blocks. For example, with the increasing shear rate, the normal boundary condition of a shallow-buried rough discontinuity would change from the constant normal stress condition to the constant normal stiffness condition, due to the "hardening" of surrounding rock blocks [8]. However, the shear process of asperities on joint surfaces is not a pure tension or shear process. Up to now, the understanding of shear rate effects on rough joints is still at its infancy as multiple failure models co-exist during shearing, e.g., frictional sliding, surface wearing and asperity cracking etc.[21].

Due to the complexity of the shear mechanism, many scholars tended to build dynamic joint constitutive models by introducing a rate-related component into static/quasi-static models. Two typical methods were usually adopted. One method introduces the rate-related component in the form of multiplication, suggesting that the rate-dependent effect could be totally reflected by material constants [22]. For example, to reflect the time-dependent friction behaviour of joints, Kana *et al.* [23] directly modified the interlock-friction function by multiplying its frictional term with an amplification factor; Cui *et al.* [24] proposed a rate-dependent joint model in consideration of rate-dependent shear stiffness, where the ratio of the dynamic to static stiffness was expressed by an exponential function. The other method introduces the rate-related component in the form of addition, suggesting that the total force/displacement is the sum of the static (rate-independent) component and the dynamic (rate-dependent) component [25]. For example, Schneider [2] conducted a series of friction tests on clay rock joints and stated that frictional force can be divided into a linear elastic part and a viscoplastic part; Zhu *et al.* [26] and Zhu *et al.* [27] examined dynamic responses of rock joints and proposed that the overall strain rate can be divided into a viscous portion and an elastic portion. Unfortunately, regardless of addition or multiplication, the applicability of the dynamic joint models mentioned above is strongly dependent on the validity of the adopted static/quasi-static models. Usually, these static models are not suitable for the shear phases after shear strength, thus they are unable to reflect the whole shear process of joints [28].

The objectives of this study are to investigate the joint shear behaviour at different shear rates, and to propose a rate-dependent constitutive model for incorporating the whole shearing process of joints. A series of laboratory tests of artificial rough joints were firstly conducted at shear rates of 1 mm/s and 10 mm/s. The influence of shear rates on the shear process was then analyzed and formulated by two excess stress models. The underlying mechanism behind the two models

relevant to shear rate effects was analyzed and then validated by a series of numerical tests. The findings in this paper could add substantially to our knowledge about the rate-dependent shear behaviour of rough joints and provide an analytical framework to correlate the dynamic shear behaviour of joints with the static/quasi-static one.

2 Experimental set-ups

2.1 Sample preparation

Mated mortar joints were prepared to examine the shear behaviour of rough joints at different shear rates. Mortar was selected to simulate rock materials in our study due to its rock-like properties and temperature stability [3, 29-32]. In our study, a mix of water, cement and sand in the proportion of 0.4:1:1.5 by weight was adopted to simulate the rock material with the uniaxial compression strength of about 34 MPa and the Young's modulus of about 7.95 GPa. After casting and curing, the exterior surfaces of the specimens were ground parallel and flat to ensure uniform normal and shear loadings. The final dimensions of the joint samples are about 100 mm in length, 100 mm in width, and 100 mm in height.

Fig. 1 shows profiles of the rough joints used in thus study. Three types of rough joints were prepared by using the same mortar material, but the contact surfaces in the middle of the mold were different. Fig. 1a shows samples with irregular triangular asperities, fabricated to simulate joints with multi-scale unevenness. The shear behaviour of these joints is influenced seriously by the interaction between asperities [33]. Fig. 1b shows samples with regular triangular asperities, which were prepared to simulate joints with periodic waviness/unevenness. The shear behaviour of those joints is dominated by the deformation or failure of asperities [33]. Besides, samples with unpolished planar surfaces were also prepared to simulate joints with meso-roughness, as shown in Fig. 1c, along which frictional characteristics are significant.

2.2 Experimental setup

Shear experiments were conducted under constant normal load conditions by using an instrumented direct shear testing system in Institute of Geology and Geophysics, Chinese Academy of Sciences, as shown in Fig. 2. The testing system consists of four components, i.e., the hydraulic aggregate, the air pressure accumulators, the shear box with horizontal and vertical frames, and the electronic control unit. The detachable upper and lower shear boxes can move

freely in the horizontal and vertical directions, respectively. Two small and five large air pressure accumulators were employed to provide the energy for dynamic loadings. Four linear variable differential transducers (LVDTs) were put on four corners at the top of the shear box to measure the normal displacement. Two LVDTs were placed in parallel to the lower shear box to measure the shear displacement. Details of this testing system were reported by Qi *et al.* [34] and Zheng *et al.* [35].

In our tests, joint specimens were tested at shear rates of 1 mm/s and 10 mm/s, i.e., at strain rates of 10^{-2} s^{-1} and 10^{-1} s^{-1}, and under normal stresses of 1 MPa, 3 MPa and 5 MPa, respectively. Normal stress was maintained constantly during shearing. Different shear rates were applied through a standard displacement-controlled procedure suggested by Zheng [36]. Both shear displacement and stress were recorded automatically during the shearing process.

3 Testing results and analysis

3.1 The influence of shear rate

Fig. 3 illustrates shear stress-shear displacement responses of the unpolished planar joints at shear rates of 1 mm/s and 10 mm/s under varied normal stresses, i.e., 1 MPa, 3 MPa and 5 MPa. It could be found that shear/frictional strength is insensitive to the shear rates ranging from 1 mm/s to 10 mm/s, that is, shear rate effects on the unpolished planar joints with meso-roughness are slight in terms of shear strength at these shear rates.

Figs. 4 and 5 show shear stress-displacement responses of the joints with regular and irregular asperities, respectively. Shear rates applied were 1 mm/s and 10 mm/s under varied normal stresses, i.e., 1 MPa, 3 MPa and 5 MPa. It can be seen that peak shear strength increases with the rise of shear rates. The magnitude of the strength increment is dependent on the normal stress applied. For the joints with regular asperities, relative strength changes as the shear rate rises from 1 mm/s to 10 mm/s were about 45%, 26% and 12% under normal stresses of 1 MPa, 3 MPa and 5 MPa, respectively. For joints with irregular asperities, the change in strength decreases to 27% under 1 MPa, 11% under 3 MPa and 7% under 5 MPa.

Interestingly, the rate-independent behaviour can be also observed in the tests on the joints with regular and irregular asperities. As shown in Figs. 4 and 5, final residual stresses of the joints with regular and irregular asperities appear to approach kinetic frictional strengths of the planar joints, when shear displacements are large enough. The periodic stress fluctuation in the residual strength

phase reflects the continuous wearing and grinding of the small fragments between joint surfaces. Similar to the friction/shear process of planar joints, this wearing/grinding process can also be considered as continuous damaging and breaking of meso-roughness. This concept is in line with the findings of Zhao [37], who suggested that joint shear strength changes with loading rates due to the rate-dependence cohesion, and friction angle seems unaffected by loading rates.

From Figs. 3, 4 and 5, it could be concluded that joint shear rate effects are influenced by joint roughness. In our study, the largest difference in shear strength was achieved under the normal stress of 1 MPa. For planar joints, the relative change in strength is negligible at 5%. For the joints with macro-unevenness, this strength change rises to around 45% for regular asperities and 27% for irregular asperities. The difference in the extent of shear rate effects may be relevant to the actual number of the asperities in contact when the shear strength is reached. For planar joints, there is no macro-asperities. Shear rate effects thus seem to be negligible. For the joints with irregular asperities, because of the stress transfer among asperities [28], only the steepest asperities get contacted when the peak stress is reached. Thus, an obvious increase in strength was observed. For the joints with regular asperities, all the asperities remain contacted until the peak stress is reached. Thereby, shear rate effects become significant.

It should be noticed that the stress fluctuation in the residual strength phase is more significant at higher shear rates. For instance, under the normal stress of 5 MPa, the shear resistance of the joint with irregular asperities at the shear rate of 10 mm/s (Irregular-5-10) shows obvious fluctuations in the residual strength phase, while there is hardly any fluctuation at 1 mm/s (Irregular-5-1). This difference indicates that the continuous breaking of fragments is more intense at a higher shear rate. Besides, it can be seen from Figs. 4 and 5 that, at the shear rates of 1 mm/s and 10 mm/s, the displacements at shear strength are almost the same. For example, under the normal stress of 1 MPa, the shear displacement of the joint with irregular asperities at the shear rate of 1 mm/s (Irregular-1-1) is 1.96 mm, while the corresponding displacement at the shear rate of 10 mm/s (Irregular-1-10) is 2.25 mm. The relative difference is less than 15%. When normal stress increases to 5 MPa, the relative difference decreased to around 3%. Furthermore, the shear displacements at the end of the first stress drop, i.e., at the beginning of the residual strength phase, also keep constant with the increase of the applied shear rate. For instance, the displacements at the end of the first stress drop for Sample “Irregular-1-1” and Sample “Irregualr-1-10” are

approximately 8.7 mm and 9.5 mm, respectively. The relative difference is about 9%. When normal stress increases to 5 MPa, the relative difference decreased to approximately 2%.

3.2 Four shear phases of rough joints

To quantitatively characterize the shear behaviour of rough joints, the shear process of joints with regular and irregular asperities was divided into four phases, i.e., linear elastic phase, shear hardening phase, shear softening phase, and residual strength phase. as shown in Fig. 6. In the linear elastic phase, shear stress linearly increases until reaching the initial yield limit (τ^*), which approximately equals to the residual strength of the joint [38]. Shear stiffness here is considered constant and called "linear stiffness (k_{lin})" [38]. The shear stress-shear displacement curve seems step-shaped in this phase, due to the sudden compression of the interspace between the specimen and the shear box. In the shear hardening phase, shear stress increases, while shear stiffness decreases continuously. The total shear displacement in this phase is denoted as "a_h", which defines the hardening behaviour of the joint. In the shear softening phase, shear stress falls from the peak to the residual strength [28, 39]. Shear stiffness becomes negative. The total shear displacement in this phase is denoted as "a_s", which defines the softening behaviour of the joint. In the residual strength phase, shear stress periodically fluctuates and finally approaches the kinetic frictional resistance of planar joints. To simplify the discussion, this periodical stress fluctuation, resulting from continuous grinding of fragments, is ignored in the present study. Shear stiffness thus equals to zero in this phase. The residual strength (τ_r) here is considered equal to the initial yield limit (τ^*).

Within the four phases, five controlling parameters were extracted to describe the joint shear behaviour: the initial yield limit (τ^*), the peak strength (τ_p), the linear stiffness (k_{lin}), the shear-displacement increments in the hardening and softening phases (a_h & a_s).

4 A rate-dependent constitutive model of rough joints

As discussed above, the shear process of rough joints was divided into four phases and characterized by five controlling parameters. Here, τ^*, k_{lin}, a_h and a_s are considered to be rate-independent at shear rates from 1 mm/s to 10 mm/s. τ_p is treated to be rate-dependent and regarded as the most important variable reflecting shear rate effects. This simplification emphasizes the importance of shear strength and reflects the major feature of shear rate effects, i.e., shear strength

increases with shear rates. Based on this, a one-dimensional constitutive model of rough joints was developed, which can reflect rate-dependent shear behaviour and describe the nonlinear hardening and softening processes.

The proposed model is a mechanical conceptual model based on the Hooke-Saint Venant model (Fig. 7), in which elastic and plastic elements are connected in series to gain an ideal elastoplastic response. In the new model, the Saint Venant element was modified to reflect the hardening/softening process. Fig. 8 shows sketches of the traditional and modified Saint Venant models. In the traditional one, yield strength/limit could be determined by two compressed springs installed between two parallel surfaces, as shown in Fig. 8a. By contrast, in the modified model, springs are installed between two inclining surfaces to incorporate the alterable yield strength/limit, as shown in Fig. 8b. The yield strength/limit increases under loading conditions (Fig. 8b-Model I) and decreases under unloading conditions (Fig. 8b-Model II), representing the hardening and softening processes, respectively.

To reflect rate-dependent effects of rough joints, a Newton element was added to the proposed model to introduce an additional time-related stress component under dynamic conditions. Fig. 9 shows sketches of the Hooke-modified Saint Venant/Newton (H-S_m/N) model and the Hooke/Newton-modified Saint Venant (H/N-S_m) mode, which are proposed with consideration of the underlaying mechanism of crack initiation. In shear hardening phase, since microcrack initiation is attributed to the accumulation of plastic deformations [28, 38], the Newton model is placed in parallel with the modified Saint Venant model to achieve an elastic-viscoplastic response, as shown in Fig. 9a. For shear softening phase, as microcrack initiation results from the energy release of elastic deformation [28, 39], the Newton model is connected in parallel with the Hooke model to achieve an elastoviscous-plastic response, as shown in Fig. 8b.

In fact, these two models are both excess stress models. Stress increments of the two models can be divided into rate-independent and rate-dependent components. Particularly, when the strain rate of the Newton model maintains constant, stress increments in these two models both come from the Hooke and Modified Saint Venant models, rather than the Newton model. The overall stiffness at this time would not be influenced by the strain/deformation rate, i.e., it is rate-independent. In contrast, when the strain rate of the Newton model becomes alterable, the stress increment would be affected by the Newton model; the overall stiffness would be a function of strain/deformation rate, i.e., it is rate-dependent. Therefore, the two models have the nature to

reflect both rate-independent and rate-dependent behaviour of rough joints. In other words, joint deformation under static or quasi-static conditions could be represented by the Hooke-modified Saint Venant (H-S_m) model, while rate-dependent effects under dynamic conditions could be reflected by the H-S_m/N model or the H/N -S_m model.

Therefore, with the modified Saint Venant model and the properly emplaced Newton element, the shear hardening and softening behaviour of rough joints under dynamic conditions could be described by two excess stress models. The hardening process could be described by the H-S_m/N model in compression and the shear softening process could be described by the H/N -S_m model in tension. Details of the two models are presented below.

4.1 The H-S_m/N model

For the Hooke element [39]:

$$d\tau_H = k_1 du_H \quad (1)$$

where du_H and $d\tau_H$ are displacement and stress increments, respectively; k_1 is the spring stiffness, which is taken positive under compressive/loading conditions.

For the modified Saint Venant element [28]:

$$d\tau_{M\_S} = 2k_2 \tan\theta \tan(\varphi \pm \theta) du_{M\_S} \quad (2)$$

where du_{M_S} and $d\tau_{M\_S}$ are displacement and stress increments, respectively; θ and φ are the dip angle and fictional angle of the frictional surfaces, respectively; k_2 denotes spring stiffness; plus and minus here represent loading and unloading conditions, respectively.

For the Newton element (Jaeger et al., 2009):

$$\tau_N = \eta \frac{du_N}{dt} \quad (3)$$

$$\frac{d\tau_N}{dt} = \eta \frac{d^2 u_N}{dt^2} = \eta \frac{d\dot{u}_N}{dt} \quad (4)$$

where $d\tau_N$, du_N and $d\dot{u}_N$ are stress, displacement and velocity increments, respectively; t is time, which is renamed as the equivalent time in the H-S_m/N model; η is the dynamic viscosity with the unit of $MPa \cdot S/mm$.

Since the Newton element is connected in parallel with the modified Saint Venant element, the basic characteristics of the H-S_m/N model should satisfy the following equations:

$$d\tau_T = d\tau_H = d\tau_{M\_S} + d\tau_N \quad (5)$$

$$du_{M\_S} = du_N \quad (6)$$

$$du_T = du_H + du_{M\_S} = du_H + du_N \quad (7)$$

where $d\tau_T$ and du_T are the total stress and displacement increments, respectively. The two parameters can be rewritten by bringing Eqs. (1)-(4) into Eqs. (5) and (7). There are:

$$d\tau_T = k_1 du_H = 2k_2 \tan\theta \tan(\varphi+\theta) du_{M\_S} + \eta d\dot{u}_N \quad (8)$$

$$du_T = \frac{\left[k_1 + 2k_2 \tan\theta \tan(\varphi+\theta)\right] du_N + \eta d\dot{u}_N}{k_1} \quad (9)$$

Thus, the stiffness of the H-S_m/N model could be derived:

$$k_d = \frac{d\tau_T}{du_T} = \frac{2k_1k_2 \tan\theta \tan(\varphi+\theta)\frac{du_N}{dt} + \eta k_1 \frac{d^2u_N}{dt^2}}{\left[k_1 + 2k_2 \tan\theta \tan(\varphi+\theta)\right]\frac{du_N}{dt} + \eta \frac{d^2u_N}{dt^2}} \quad (10)$$

Eq. (10) represents the shear stiffness evolution of rough joints in the hardening phase. Here, dynamic shear stiffness k_d is a function of du_N/dt, indicating that the shear stiffness of rough joints is related to strain history under dynamic conditions. When d^2u_N/dt^2 equals to zero, k_d in Eq. (10) degrades into the static stiffness k_s, that is:

$$k_s = \frac{2k_1k_2 \tan\theta \tan(\varphi+\theta)}{k_1 + 2k_2 \tan\theta \tan(\varphi+\theta)} \quad (11)$$

According to Eq. (7), the rate-related characteristic of the H-S_m/N model should satisfy the following equation, which defines the hardening rule of rough joints under dynamic conditions:

$$\frac{du_T}{dt} = \frac{du_H}{dt} + \frac{du_{M\_S}}{dt} = \frac{du_H}{dt} + \frac{du_N}{dt} = v_s \quad (12)$$

where v_s is the shear rate.

Substituting Eq. (8) into Eq. (12), we have:

$$\frac{\left[k_1 + 2k_2 \tan\theta \tan(\varphi+\theta)\right]}{k_1}\frac{du_N}{dt} + \frac{\eta}{k_1}\frac{d^2u_N}{dt^2} = v_s \quad (13)$$

Thus, the following equation could be derived:

$$\frac{du_N}{dt} = C_1 \exp\left(-\frac{\left[k_1 + 2k_2 \tan\theta \tan(\varphi+\theta)\right]t}{\eta}\right) + \frac{k_1 v_s}{k_1 + 2k_2 \tan\theta \tan(\varphi+\theta)} \quad (14)$$

where C_1 is a constant.

Here, t in the H-S_m/N model is not the "real" time measured in our tests. Eqs. (1)-(4) were derived in the incremental form algorithm, indicating that Eq. (14) was derived without regard to the total displacement. Therefore, t can be reckoned as a state variable in the H-S_m/N model, reflecting the effect of strain history. In the present study, t is treated as a function of "real" time (i.e., $t = f(u_T / v_s)$) and renamed "equivalent time" thereafter.

Bringing Eq. (13) into Eq. (10), the dynamic shear stiffness k_d is expressed as:

$$k_d = k_1 - \frac{k_1}{v_s}\frac{du_N}{dt} \quad (15)$$

Notably, at the beginning of the hardening phase, there is no irreversible/plastic deformation [38]. Thus, both t and du_N/dt equal to zero. k_d equals to k_{1in}. Accordingly, C_1 in Eq. (14) is expressed as:

$$C_1 = -\frac{k_{lin} v_s}{k_{lin} + 2k_2 \tan\theta \tan(\varphi + \theta)} \quad (16)$$

At the end of the hardening phase, shear stress peaks. k_d decreases to zero. Therefore, du_N/dt in Eq. (15) equals to v_s, indicating that rate-dependent effects become negligible. Here, t tends to become infinite, and Eq. (14) is rate-independent, that is:

$$\frac{du_N}{dt} = \frac{k_{lin} v_s}{k_{lin} + 2k_2 \tan\theta \tan(\varphi + \theta)} = v_s \quad (17)$$

To make Eq. (17) valid, we found that θ and φ in the H-S_m/N model can be defined by the following equations:

$$\tan\theta = \frac{a_h - \Delta u_h}{A_h} \quad (18)$$

$$\tan\varphi = \frac{A_h}{a_h} \quad (19)$$

where a_h is the total displacement in the nonlinear hardening phase, as shown in Fig. 6; Δu_h is the relative shear displacement, which changes from zero to a_h; A_h is an empirical constant with unit of *mm*.

Bringing Eqs. (18) and (19) into Eq. (17), the value of A_h could be directly derived. Therefore, k_d in Eq. (15) would be rewritten as:

$$k_d = \frac{2k_{lin}k_2\left(a_h - \Delta u_h\right)\left(1 + a_h{}^2 - \Delta u_h a_h\right) + k_{lin}{}^2 \Delta u_h f\left(\Delta u_h, v_s\right)}{k_{lin}\Delta u_h + 2k_2\left(a_h - \Delta u_h\right)\left(1 + a_h{}^2 - \Delta u_h a_h\right)} \left(0 < \Delta u_h \le a_h\right) \quad (20)$$

$$f\left(\Delta u_h, v_s\right) = \exp\left(-\frac{k_{lin}\Delta u_h t + 2k_2 t(a_h - \Delta u_h)(1 + a_{\mathrm{h}}{}^2 - \Delta u_h a_{\mathrm{h}})}{\eta \Delta u_h}\right) \in [0,1];\ t = f\left(\frac{\Delta u_h}{v_s}\right) \quad (21)$$

However, the indefinite integral of $f\left(\Delta u_h, v_s\right)$ with respect to Δu_h cannot be expressed by any elementary function. For the convenience of calculation, we simplified Eq. (21) and redefined that:

$$f\left(\Delta u_h, v_s\right) = \left(\frac{a_h - \Delta u_h}{a_h}\right)^{\frac{\eta^*}{v_s}} \in [0,1] \quad (22)$$

where η^* is a viscosity-related material constant with the unit of *mm/s*, which is inversely proportional to η. The rationality of substituting Eq. (22) for Eq. (21) will be discussed later. When v_s becomes infinitely small, k_s (static stiffness) would be directly derived from Eqs. (20) and (22):

$$k_s = \frac{2k_{lin}k_2\left(a_h - \Delta u_h\right)\left(1 + a_h{}^2 - \Delta u_h a_h\right)}{k_{lin}\Delta u_h + 2k_2\left(a_h - \Delta u_h\right)\left(1 + a_h{}^2 - \Delta u_h a_h\right)} \left(0 < \Delta u_h \le a_h\right) \quad (23)$$

4.2 The H/N-Sm model

Since the Newton model is connected in parallel with the Hooke model, the basic characteristics of the H/N-S_m model under unloading conditions should satisfy:

$$d\tau_T = d\tau_{M\_S} = d\tau_H - d\tau_N \quad (24)$$

$$du_H = du_N \quad (25)$$

$$du_T = du_H + du_{M\_S} = du_N + du_{M\_S} \quad (26)$$

The total stress increment and displacement increment are:

$$d\tau_T = 2k_2^{'} \tan\theta \tan(\varphi - \theta) du_{M\_S} = k_1^{'} du_H - \eta d\dot{u}_N \quad (27)$$

$$du_T = \frac{\left[k_1^{'} + 2k_2^{'} \tan\theta \tan(\varphi - \theta)\right] du_N - \eta d\dot{u}_N}{2k_2^{'} \tan\theta \tan(\varphi - \theta)} \quad (28)$$

where k_1' and k_2' are spring stiffnesses in the Hook and modified Saint Venant models, respectively. They are taken negative under unloading conditions. Since elastic constants are often considered invariable in the plastic/irreversible deformation phase, the absolute value of k_1' in Eq. (28) equals to k_{lin} by definition.

The stiffness of the H/N-S_m model is then derived:

$$k_d = \frac{d\tau_T}{du_T} = \frac{2k_{lin}k_2^{'}\tan\theta\tan(\varphi-\theta)\frac{du_N}{dt} - 2\eta k_2^{'}\tan\theta\tan(\varphi-\theta)\frac{d^2u_N}{dt^2}}{\left[k_{lin}+2k_2^{'}\tan\theta\tan(\varphi-\theta)\right]\frac{du_N}{dt} - \eta\frac{d^2u_N}{dt^2}} \quad (29)$$

Eq. (29) determines the evolution of shear stiffness in the softening phase. Similar to the H-S_m/N model, when d^2u_N/dt^2 equals to zero, k_d degrades into k_s, that is the stiffness of the H-S_m model:

$$k_s = \frac{2k_{lin}k_2^{'}\tan\theta\tan(\varphi-\theta)}{k_{lin}+2k_2^{'}\tan\theta\tan(\varphi-\theta)} \quad (30)$$

According to Eq. (17), the rate-related characteristic of the H/N-S_m model should satisfy:

$$\frac{du_{M\_S}}{dt} = v_s \quad (31)$$

Substituting Eq. (27) into Eq. (31), there is :

$$\frac{k_{lin}}{2k_2^{'}\tan\theta\tan(\varphi-\theta)}\frac{du_N}{dt} - \frac{\eta}{2k_2^{'}\tan\theta\tan(\varphi-\theta)}\frac{d^2u_N}{dt^2} = v_s \quad (32)$$

Thus,

$$\frac{du_N}{dt} = C_2\exp(\frac{k_{lin}t}{\eta}) + \frac{2v_sk_2^{'}\tan\theta\tan(\varphi-\theta)}{k_{lin}} \quad (33)$$

where C_2 is a constant.

Bringing Eq. (32) into Eq. (29), we have:

$$k_d = \frac{2v_sk_2^{'}\tan\theta\tan(\varphi-\theta)}{v_s+\frac{du_N}{dt}} \quad (34)$$

At the beginning of the softening phase, the elastic potential energy stored has not been released yet [40]. Both t and du_N/dt should equal to zero. Thus, C_2 is derived:

$$C_2 = -\frac{2v_sk_2^{'}\tan\theta\tan(\varphi-\theta)}{k_{lin}} \quad (35)$$

Eq. (34) should satisfy:

$$k_d = 2k_2^{'}\tan\theta\tan(\varphi-\theta) = 0 \quad (36)$$

At the end of the softening phase, the elastic potential energy will be fully released. The effect of the Newton element here becomes negligible. Thus, t tends to become infinite and Eq. (33) could be rewritten as:

$$\frac{du_N}{dt} = \frac{2v_s k_2^{'} \tan\theta \tan(\varphi - \theta)}{k_{lin}} = 0 \quad (37)$$

To make Eq. (36) and (37) valid, we found that θ and φ in the H/N-S_m model must follow:

$$\tan\theta = \frac{\Delta u_s}{A_s} \quad (38)$$

$$\tan\varphi = \frac{a_s}{A_s} \quad (39)$$

where a_s is the total displacement at the shear softening stage, as shown in Fig. 6; Δu_s is the relative shear displacement, ranging from zero to a_s; A_s is an empirical constant with the unit of *mm*.

Bringing Eqs. (38) and (39) into Eq. (37), A_s could be directly derived. Therefore, k_d in Eq. (34) can be rewritten as:

$$k_d = \frac{2k_{lin}k_2^{'}\Delta u_s(a_s - \Delta u_s)}{k_{lin}(1 + a_s\Delta u_s) + 2k_2^{'}\Delta u_s(a_s - \Delta u_s) - 2k_2^{'}\Delta u_s(a_s - \Delta u_s) f(\Delta u_s, v_s)} \ (0 < \Delta u_s \le a_s) \quad (40)$$

$$f(\Delta u_s, v_s) = \exp(k_{lin}t/\eta) \in [0,1];\ t = f(\frac{\Delta u_s}{v_s}) \quad (41)$$

Similar to the H-S_m/N model, we adopted a similar approximation to the exponential term in Eq. (41):

$$f(\Delta u_s, v_s) = \left(\frac{a_s - \Delta u_s}{a_s}\right)^{\frac{\eta^*}{v_s}} \in [0,1] \quad (42)$$

When v_s tends to be infinitely small, k_s could be derived directly from Eqs. (40) and (42):

$$k_s = \frac{2k_{lin}k_2^{'}\Delta u_s(a_s - \Delta u_s)}{k_{lin}(1 + a_s\Delta u_s) + 2k_2^{'}\Delta u_s(a_s - \Delta u_s)} \ (0 < \Delta u_s \le a_s) \quad (43)$$

4.3 The rate-dependent model of rough joints

With the two excess stress models, i.e., the H-S_m/N model and H/N-S_m model, the stiffness evolution in hardening and softening phases can be expressed mathematically. Here, we combined

them together and defined a piecewise function as the final shear constitutive model of rough joints, that is:

$$k_d = \begin{cases} k_{lin} & \text{linear elastic phase} \\ \dfrac{2k_{lin}k_2\left(a_h-\Delta u_h\right)\left(1+{a_h}^2-\Delta u_h a_h\right)+{k_{lin}}^2\Delta u_h f\left(\Delta u_h, v_s\right)}{k_{lin}\Delta u_h+2k_2\left(a_h-\Delta u_h\right)\left(1+{a_h}^2-\Delta u_h a_h\right)} & \text{the hardening phase} \\ \dfrac{2k_{lin}k_2'\Delta u_s(a_s-\Delta u_s)}{k_{lin}(1+a_s\Delta u_s)+2k_2'\Delta u_s(a_s-\Delta u_s)-2k_2'\Delta u_s(a_s-\Delta u_s)f\left(\Delta u_s, v_s\right)} & \text{softening phase} \\ 0 & \text{residual strength phase} \end{cases} \tag{44}$$

where

$$f\left(\Delta u_h, v_s\right)=\left(\frac{a_h-\Delta u_h}{a_h}\right)^{\frac{\eta^*}{v_s}} \text{ and } f\left(\Delta u_s, v_s\right)=\left(\frac{a_s-\Delta u_s}{a_s}\right)^{\frac{\eta^*}{v_s}}$$

$0<\Delta u_h \le a_h$ and $0<\Delta u_s \le a_s$

Eq. (44) determines the stiffness evolution during the whole shearing process, indicating that static and dynamic shear stiffnesses of joints could be correlated by a rate-dependent component, i.e., $f\left(\Delta u_h, v_s\right)$ or $f\left(\Delta u_s, v_s\right)$. From Eq. (44), we can easily derive the static shear stiffness by setting the shear rate to be infinitely small, there is:

$$k_s = \begin{cases} k_{lin} & \text{linear elastic phase} \\ \dfrac{2k_{lin}k_2\left(a_h-\Delta u_h\right)\left(1+{a_h}^2-\Delta u_h a_h\right)}{k_{lin}\Delta u_h+2k_2\left(a_h-\Delta u_h\right)\left(1+{a_h}^2-\Delta u_h a_h\right)} & \text{hardening phase} \\ \dfrac{2k_{lin}k_2'\Delta u_s(a_s-\Delta u_s)}{k_{lin}(1+a_s\Delta u_s)+2k_2'\Delta u_s(a_s-\Delta u_s)} & \text{softening phase} \\ 0 & \text{residual strength phase} \end{cases} \tag{45}$$

where

$0<\Delta u_h \le a_h$ and $0<\Delta u_s \le a_s$

It is noteworthy that there are only five parameters in the static/quasi-static model: a_h, a_s, k_{lin}, k_2 and k_2'. Here, k_{lin}, k_2 and a_h define the hardening process of rough joints, and k_{lin}, k_2', and a_s characterize the softening process. Values of the model parameter can be obtained based on Eq. (45) by best fitting with the static shear stress-displacement curve. Then, dynamic shear behaviour

of the joint can be predicted by Eq. (44) on the basis of the obtained values of fitting parameters and the given shear rate.

5 Applicability of the rate-dependent model of rough joints

Fig.10 shows the shear stress-displacement relationship of joints with regular asperities obtained from the proposed model and the laboratory tests at shear rates of 1 mm/s and 10 mm/s. The fitting curves were obtained based on the static shear stiffness model, i.e., Eq. (45). Here, k_{lin}, a_h and a_s were measured directly from the stress-displacement curves, and values of k_2 and k_2' were obtained through a trial-and-error process. The predicted curves were obtained based on Eq. (44) according to the obtained values of fitting parameters and the given shear rate. Table 1 lists the values of parameters used in the proposed joint model. The viscosity-related constant η^* was set to 10 mm/s for the mortar joints in the present study and assumed to be independent on the shear rate from 1 mm/s to 10 mm/s. This value was determined by trial and error based on the testing results of the joints with regular asperities under normal stresses of 1 MPa and 5 MPa.

It can be seen from Fig. 10 that the nonlinear stress-displacement relationship of the joints at the shear rate of 10 mm/s were predicted successfully by the testing results of the joints at the shear rate of 1mm/s. Although the direct shear tests were conducted only at shear rates of 1 mm/s and 10 mm/s, the agreement between laboratory measurements and predicted results proves the applicability of the proposed joint model. Noteworthy, the fitting and predicted curves do not start from the origin. We ignored the step-shaped section of the curves, as it results from the gap between the joint specimen and the inner surface of the shear box.

Fig.11 shows the shear stress-displacement relationship of joints with irregular asperities obtained from the proposed model and the laboratory tests at shear rates of 1 mm/s and 10 mm/s. Values of parameters used in the proposed model was listed in Table 2. In Fig. 11, the nonlinear stress-displacement relations at the shear rate of 10 mm/s were predicted successfully by the fitting curves at the shear rate of 1mm/s. Noteworthy, under the same loading conditions, the residual strengths at shear rates of 1 mm/s and 10 mm/s both approached the kinetic friction strength of planar joints.

Therefore, the predicted results from joints with regular and irregular asperities suggest that this one-dimensional constitutive model of rough joints is able to successfully reflect the dynamic shear

behaviour of rough joints, including the rate-dependent shear strength and the nonlinear hardening and softening processes.

6 The mechanism of shear rate effects

As stated in Section 4, when the strain rate of the Newton model maintains constant, the transient stress increment of the H-Sm/N model only comes from the Hooke and the modified Saint Venant models. The total stiffness would not be influenced by strain/deformation rate, i.e., it is rate-independent. In contrast, when the strain rate of the Newton model is not a constant, the deformation of the H-Sm/N model would be affected by the damping from the Newton element. The total stiffness here is rate-dependent. Therefore, shear rate effects of rough joints represented by the H-Sm/N model are correlated with the strain rate of irrecoverable deformation. Here, we introduced a hypothesis to explain this mechanism: microcrack propagation is relatively steady under static conditions but becomes increasingly unstable with the rise of shear rate. This hypothesis is coincident with phenomenological statements for strain rate effects from Cadoni *et al.* [41] and Gillette *et al.* [6]. After conducting a series of static and dynamic tensile tests on intact concrete samples, Cadoni *et al.* [41] found that the major tensile mechanism of concrete changes from ductile inter-granular fracturing at low strain rates to brittle trans-granular fracturing at high strain rates, indicating that energy dissipation for cracking varies with the type of crystal particles and contributes to unstable crack expansion at high shear rates. Gillette *et al.* [6] conducted many direct shear tests on intact sandstones and found that more than one cracks would be activated under dynamic conditions, indicating that different cracking processes would be superimposed during shearing, causing unstable deformation and failure. In fact, this multiple-cracking phenomenon was widely observed in both compression, tension and shear tests of rock or rock-like materials [42-46].

To verify this hypothesis about shear rate effects of rough rock joints, we conducted a series of numerical direct shear tests of joints with irregular asperities by the particle flow code (PFC-2D). The numerical tests were conducted under the same loading conditions as the laboratory tests did. If the hypothesis is correct, the number of microcracks generated during shearing would be shear-rate dependent.

Fig. 12 shows the geometric model used in numerical shear tests. Joint walls were simulated by the dense assembly of particles bonded by the parallel bond model and joint surfaces were

represented by the smooth joint contact model [47-49]. The geometric model was built by the shear box genesis approach, which was introduced by Bahaaddini *et al.* [47]. With this method, particles in the upper and lower blocks were separately generated. The intended joint plane was added as a common boundary named "contact surfaces". Crucially, in our study, particles in the upper and lower blocks were generated with different size ranges to alleviate the periodic fluctuation in contact number during shearing. This method has been detailed by Li *et al.* [50]. The nominal size of this geometric model is 100×50 mm. Its thickness is smaller than that of the mortar joints used in experiment tests. This simplification reduces the number of particles and saves computing time without reducing computational accuracy [47].

Table 3 lists the values of the model parameters adopted in the PFC modelling, which were calibrated with two planar mortar joints as well as five cylindrical mortar samples through a standard calibration procedure introduced by Bahaaddini [51]. The parameters of the smooth joint contact model were calibrated by direct shear and normal compression tests of planar mortar joints, which were composed of two cube mortar blocks with the nominal size of 100×100×100 mm and the contact area of 100×100 mm^2. The parameters of the parallel bond model were calibrated based on a series of uniaxial compression tests of cylindrical mortar samples with the diameter of 50 mm and the height of 100 mm. The uniaxial compressive strength, the Young's modulus and the Poisson's ratio of the simulated mortar material are 34 MPa, 7.95 GPa and 0.21, respectively. Energy dissipation in the numerical tests was determined by the value of local damping, which was set to 0.015 according to the suggestion from Hazzard *et al.* [52].

Fig. 13 shows the evaluation of shear stress and crack number as a function of shear displacement during shearing, where the normal stresses applied were 5 MPa. The shear rates applied in the laboratory tests were 1 mm/s and 10 mm/s, while the shear rates applied in the numerical simulations were 1mm/s, 10 mm/s and 100 mm/s. To eliminate the influence of the gap between the joint sample and the shear box, the horizontal coordinate starts from 1.4 mm. Results shows that numerical modelling results agree well with laboratory testing results with respect to the peak shear stress, the residual strength and the shear displacement at peak stress, suggesting that the accuracy of the numerical modelling is acceptable.

It can be seen from Fig. 13 that although crack number increases with the increasing shear displacement, a clear difference exists at three different shear rates. At the shear rate of 1 mm/s, the number of cracks increased steadily before the shear strength was reached. At the shear rate of

10 mm/s, the number of microcracks increased gradually at the early stage of shearing and experienced a sharp increase near the peak shear stress. At the shear rate of 100 mm/s, the number of microcracks increased slowly at first, but jumped near the shear strength. These results indicate that crack propagation becomes more and more unstable with the increase of shear rate. Therefore, the introduced hypothesis about the mechanism of shear rate effects, that shear rate effects of rough joints are attributed to more unstable propagation of microcracks with increasing shear rate, was successfully proved by the numerical modelling results. In fact, the proposed mechanism of shear rate effects of rough joints is in accordance with the conclusion drawn by Hazzard *et al.* [52]. Hazzard *et al.* [52] utilized PFC modelling to investigate crack propagation in the uniaxial compression tests of Lac du Bonne granite samples and found that cracking forms uniformly in a highly damped model, i.e., under static conditions.

7 Discussion

In the H-Sm/N model introduced in Section 4.1, the rate-dependent exponential term, i.e., Eq. (21), was simplified to be a power function, i.e., Eq. (22). The rationality of the simplification needs to be proved. From Eq. (21), the value of the exponential term, i.e., $f(\Delta u_h, v_s)$, increases with the rise of η, indicating that the stiffness of the H-Sm/N model, expressed by Eq. (20), is inversely proportional to η^*. Fig. 14 shows the predicted shear stiffness-shear displacement relation in the hardening phase calculated with Eqs. (20) and (22) adopting different values of v_s and η^*. It is shown that when shear displacement is fixed, shear stiffness increases with increasing v_s or decreasing η^*. It should be mentioned that, in Fig. 14a, the shear stiffness-shear displacement curve at the shear rate of 0.1 mm/s overlaps with the curve under static shear conditions, where the shear rate tends to be infinitely small. Similarly, in Fig. 14b, when η^* becomes small enough, e.g., η^* equals 0.1, the degradation of shear stiffness in the hardening phase appears to be negligible. From the two figures, it can be concluded that Eq. (21) could be simplified by Eq. (22), which is capable of capturing the basic features in the evolution process of shear stiffness.

Due to the limitation of the testing apparatus, direct shear tests were conducted at shear rates up to 10 mm/s. shear dilation is not investigated because the normal displacements recorded at the four corners of the upper shear box showed inconsistent changes during shearing. This inconsistency may be attributed to the rotation of joint specimens caused by the non-uniform degradation of asperities. Only artificial joints with tooth-shaped asperities were studied in the

present study. Although the idealized unevenness is not exactly the same as the real roughness of natural joints, the obtained results could give insights into the rate-dependent shear behaviour of rough joints.

8 Conclusions

In this study, we investigate joint shear behaviour at different shear rates and develop a rate-dependent model of rough joints. Testing results show that the frictional strength of planar joints is independent on shear rates. In contrast, the shear strength of joints with macro-unevenness rises with the increase of shear rates. The residual strength of the joints appears to approach the kinetic frictional strength of planar joints, when shear displacement is large enough. Two excess stress models, i.e., the H-Sm/N model and H/N -Sm model, were developed to describe the rate-dependent shear behaviour of rough joints. The H-Sm/N model reflects the shear-stiffness evolution at hardening stage. The H/N -Sm model describes the stiffness evolution at softening stage. Both models were validated by making comparisons with laboratory measurements. Based on the proposed models, the mechanism of shear rate effects of rough joints was investigated and validated with numerical modelling. Shear rate effects are attributed to more unstable propagation of microcracks with increasing shear rates.

Acknowledgements

This research is financially supported by Supported by the Program for Guangdong Introducing Innovative and Enterpreneurial Teams (No. 2019ZT08G315), the National Science Foundation of China (Nos. U19A2098, 41661134012) and the Hong Kong Jockey Club.

References

[1] Zhang QB, Zhao J. A review of dynamic experimental techniques and mechanical behaviour of rock materials. Rock Mech. Rock Eng. 2014; 47(4): 1411-1478.
[2] Schneider H. The time dependence of friction of rock joints. Bull. Int. Assoc. Eng. Geol. 1977; 16(1): 235-239.
[3] Barton N. Non-linear shear strength for rock, rock joints, rockfill and interfaces. Innovative Infrastructure Solutions. 2016; 1(1): 30.
[4] Hencher S. Friction parameters for the design of rock slopes to withstand earthquake loading. In: Dams and Earthquake. London: Thomas Telford Publishing. 1981. pp. 74-89.
[5] Green S, Perkins R. Uniaxial compression tests at varying strain rates on three geologic materials. In: Proceedings of the 10th U.S. symposium on rock mechanics (USRMS). Austin; 20-22 May 1968. p. 254-264.

[6] Gillette DR, Sture S, Ko H-Y, Gould MC, Scott GA. Dynamic behavior of rock joints. In Proceedings of the 24th U.S. symposium on rock mechanics (USRMS). College Station; 20-23 June 1983. p. 23-32.
[7] Crawford AM, Curran JH. The influence of shear velocity on the frictional resistance of rock discontinuities. Int. J. Rock Mech. Min. Sci. Geomech. Abstr. 1981; 18(6): 505-515.
[8] Fox DJ, Kana DD, Hsiung SM. Influence of interface roughness on dynamic shear behavior in jointed rock. Int. J. Rock Mech. Min. Sci. 1998; 35(7): 923-940.
[9] Barla G, Barla M, Martinotti M. Development of a new direct shear testing apparatus. Rock Mech. Rock Eng. 2010; 43(1): 117-122.
[10] Konietzky H, Frühwirt T, Luge H. A new large dynamic rockmechanical direct shear box device. Rock Mech. Rock Eng. 2012; 45(3): 427-432.
[11] Mirzaghorbanali A, Nemcik J, Aziz N. Effects of shear rate on cyclic loading shear behaviour of rock joints under constant normal stiffness conditions. Rock Mech. Rock Eng. 2014; 47(5): 1931-1938.
[12] Atapour H, Moosavi M. The influence of shearing velocity on shear behavior of artificial joints. Rock Mech. Rock Eng. 2014; 47(5): 1745-1761.
[13] Barbero M, Barla G, Zaninetti A. Dynamic shear strength of rock joints subjected to impulse loading. Int. J. Rock Mech. Min. Sci. Geomech. Abstr. 1996; 33(2): 141-151.
[14] Barla G, Barbero M, Scavia C, Zaninetti A. Direct shear testing of single joints under dynamic loading. In: Proceedings of the international symposium on rock joints. Turin; 4 Jun 1990. p. 447-454.
[15] Jafari MK, Amini Hosseini K, Pellet F, Boulon M, Buzzi O. Evaluation of shear strength of rock joints subjected to cyclic loading. Soil. Dyn. Earthq. Eng. 2003; 23(7): 619-630.
[16] Zheng D, Li Q. An explanation for rate effect of concrete strength based on fracture toughness including free water viscosity. Eng. Fract. Mech. 2004; 71(16): 2319-2327.
[17] Barton N. Some aspects of rock joint behaviour under dynamic conditions. In: Seminar on mechanics and engineering of rocks. Torino; 23 Jan. 1988.
[18] Ragueneau F, Gatuingt F. Inelastic behavior modelling of concrete in low and high strain rate dynamics. Comput. Struct. 2003; 81(12): 1287-1299.
[19] Liao ZY, Zhu JB, Xia KW, Tang CA. Determination of dynamic compressive and tensile behavior of rocks from numerical tests of split Hopkinson pressure and tension bars. Rock Mech. Rock Eng. 2016; 49(10): 3917-3934.
[20] Zhu JB, Liao ZY, Tang CA. Numerical SHPB tests of rocks under combined static and dynamic loading conditions with application to dynamic behavior of rocks under in situ stresses. Rock Mech. Rock Eng. 2016; 49(10): 3935-3946.
[21] Grasselli G, Egger P. Constitutive law for the shear strength of rock joints based on three-dimensional surface parameters. Int. J. Rock Mech. Min. Sci. 2003; 40(1): 25-40.
[22] Johnson GR, Cook WH. Fracture characteristics of three metals subjected to various strains, strain rates, temperatures and pressures. Eng. Fract. Mech. 1985; 21(1): 31-48.
[23] Kana DD, Fox DJ. Hsiung SM. Interlock/friction model for dynamic shear response in natural jointed rock. Int. J. Rock Mech. Min. Sci. Geomech. Abstr. 1996; 33(4): 371-386.
[24] Cui Z, Sheng Q, Leng X, Ma Y. Analysis of the seismic performance of a rock joint with a modified continuously yielding model. Rock Mech. Rock Eng. 2017; 50(10): 2695-2707.
[25] Lindholm US, Yeakley LM, Nagy A. The dynamic strength and fracture properties of dresser basalt. Int. J. Rock Mech. Min. Sci. Geomech. Abstr. 1974; 11(5): 181-191.
[26] Zhu JB, Perino A, Zhao GF, Barla G, Li JC, Ma GW, Zhao J. Seismic response of a single and a set of filled joints of viscoelastic deformational behaviour. Geophys. J. Int. 2011; 186(3): 1315-1330.
[27] Zhu JB, Zhao XB, Wu W, Zhao J. Wave propagation across rock joints filled with viscoelastic medium using modified recursive method. J. Appl. Geophys. 2012; 86: 82-87.

[28] Zhu JB, Li H, Deng JH. A one-dimensional elastoplastic model for capturing the nonlinear shear behaviour of joints with triangular asperities based on direct shear tests. Rock Mech. Rock Eng. 2019; 52(6): 1671-1687.
[29] Desai C, Fishman K. Plasticity-based constitutive model with associated testing for joints. Int. J. Rock Mech. Min. Sci. Geomech. Abstr. 1991; 28(1): 15-26.
[30] Dieterich JH. Modeling of rock friction: 1. Experimental results and constitutive equations. J. Geophys. Res-Sol. Ea. 1979; 84(B5): 2161-2168.
[31] Ning Y, Zhao Z. A detailed investigation of block dynamic sliding by the discontinuous deformation analysis. Int. J. Numer. Anal. Met. 2013; 37(15): 2373-2393.
[32] Dang W, Konietzky H, Herbst M, Frühwirt T. Complex analysis of shear box tests with explicit consideration of interaction between test device and sample. Measurement, 2017; 102: 1-9.
[33] Bandis S, Lumsden AC, Barton N. Experimental studies of scale effects on the shear behaviour of rock joints. Int. J. Rock Mech. Min. Sci. Geomech. Abstr. 1981; 18(1): 1-21.
[34] Qi S, Zheng B, Wu F, Huang X, Guo S, Zhan Z, Yu Z, Barla G. A new dynamic direct shear testing device on rock joints. Rock Mech. Rock Eng. 2020; 53: 4787-4798.
[35] Zheng B, Qi S, Huang X, Guo S, Luo G. An advanced shear strength criterion for rock discontinuities considering size and low shear rate. Appl. Sci. 2020; 10(12): 4095.
[36] Zheng B, Experimental study on the dynamic shear behavior of persistent hard discontinuities. Institute of Geology and Geophysics. PhD Thesis. Chinese Academy of Sciences, Beijing; 2017.
[37] Zhao J. Applicability of Mohr–Coulomb and Hoek–Brown strength criteria to the dynamic strength of brittle rock. Int. J. Rock Mech. Min. Sci. 2000; 37(7): 1115-1121.
[38] Leong EC, Randolph MF. A model for rock interfacial behaviour. Rock Mech. Rock Eng. 1992; 25(3): 187-206.
[39] Jaeger JC, Cook NG, Zimmerman R, Fundamentals of rock mechanics(Fourth ed.). Malden MA: Blackwell Publishing; 2009.
[40] Sigenori K, Azuhiko S, Minoru K. On the mechanical behaviour of rocks under impulsive loading. Bulletin of the Faculty of engineering, Hokkaido University. 1977; 83: 51-62.
[41] Cadoni E, Labibes K, Berra M, Giangrasso M, Albertini C. High-strain-rate tensile behaviour of concrete. Mag. Concrete. Res. 2000; 52(5): 365-370.
[42] Nguyen V-M, Konietzky H, Frühwirt T. New methodology to characterize shear behavior of joints by combination of direct shear box testing and numerical simulations. Geotech. Geol. Eng., 2014; 32(4): 829-846.
[43] Zhao YX, Zhao GF, Jiang YD, Elsworth D, Huang YQ. Effects of bedding on the dynamic indirect tensile strength of coal: laboratory experiments and numerical simulation. Int. J. Coal Geol., 2014; 132: 81-93.
[44] Jiang C, Zhao GF, Zhu JB, Zhao YX, Shen LM. Investigation of dynamic crack coalescence using a gypsum-like 3D printing material. Rock Mech. Rock Eng., 2016; 49(10): 3983-3998.
[45] Ju Y, Xi CD, Zhang Y, Mao LT, Gao F, Xie HP. Laboratory in situ CT observation of the evolution of 3D fracture networks in coal subjected to confining pressures and axial compressive loads: a novel approach. Rock Mech. Rock Eng., 2018; 51(11): 3361-3375.
[46] Zhu JB, Zhou T, Liao ZY, Sun L, Li XB, Chen R. Replication of internal defects and investigation of mechanical and fracture behaviour of rock using 3D printing and 3D numerical methods in combination with X-ray computerized tomography. Int. J. Rock Mech. Min. Sci. 2018; 106: 198-212.
[47] Bahaaddini M, Sharrock G, Hebblewhite BK. Numerical direct shear tests to model the shear behaviour of rock joints. Comput. Geotech. 2013; 51: 101-115.
[48] Hu W, Kwok CY, Duan K, Wang T. Parametric study of the smooth-joint contact model on the mechanical behavior of jointed rock. Int. J. Numer. Anal. Met. 2018; 42(2): 358-376.
[49] Zhang Y, Wong LN. A review of numerical techniques approaching microstructures of crystalline rocks. Comput. Geotech. 2018; 115: 167-187.

[50] Li H, Deng JH, Yin JH, Zhu JB. Modelling the shearing behaviour of joints using an improved shear box genesis approach in particle flow code (2D) and its validation. G4. 2020; 6(1): 1-15.
[51] Bahaaddini M. Effect of boundary condition on the shear behaviour of rock joints in the direct shear test. Rock Mech. Rock Eng. 2017; 50(5): 1141-1155.
[52] Hazzard JF, Young RP, Maxwell SC. Micromechanical modeling of cracking and failure in brittle rocks. J. Geophys. Res-Sol. Ea. 2000; 105(B7): 16683-16697.

List of Tables:

List of figures:

Fig. 9 Sketches of (a) the Hooke-modified Saint Venant/Newton model and (b) the Hooke/Newton-modified Saint Venant model. k_1, k_2, k_1' and k_2' are the spring stiffness; du_H, du_{M_S} and du_N are displacement increments of Hooke, modified Saint Venant and Newton elements, respectively; θ and φ are the dip angle and fictional angle of the frictional surfaces in the modified Saint Venant element, respectively.

Fig.10 Shear stress-shear displacement curves of joints with regular asperities obtained from laboratory tests and the proposed joint model at shear rates of 1 mm/s and 10 mm/s, where the normal stress applied was: (a) 1 MPa; (b) 3 MPa; and (c) 5 MPa. The predicted curves were obtained on the basis of the fitting curves.

Fig.11 Shear stress-shear displacement curves of joints with irregular asperities obtained from laboratory tests and the proposed joint model, where the normal stress applied was: (a) 1 MPa; (b) 3 MPa; and (c) 5 MPa. The predicted curves were obtained on the basis of the fitting curves. The kinetic frictional strength of planar joints was added here to make a comparison with the residual strength of joints with irregular asperities.

Fig. 12 The geometric model of the joint with irregular asperities used in the numerical shear test. Particles in the upper and lower blocks were generated with different size ranges to alleviate the periodic fluctuation in contact number during shearing.

Fig. 13 The evolution of shear stress and crack number as a function of shear displacement from the numerical and laboratory direct shear tests of joints with irregular asperities, where the normal stresses applied were 5 MPa. The shear rates applied in the laboratory tests were 1 mm/s and 10 mm/s, while the shear rates applied in the numerical simulations were 1mm/s, 10 mm/s and 100 mm/s. To eliminate the influence of the gap between the joint sample and the shear box, the horizontal coordinate starts from 1.4 mm.

Fig. 14 The shear stiffness-shear displacement relation in the hardening phase calculated by Eqs. (20) and (22) with different: (a) v_s, and (b) different η^*. The values of model parameters are from testing results of the Sample Irregular-3-1/Irregular-3-10.

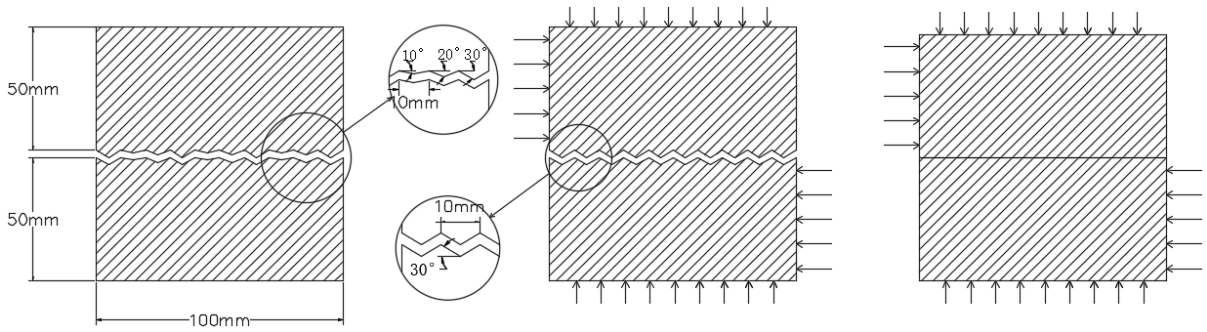

(a) (b) (c)

Fig. 1 Profiles of the mortar joint samples used in the study: (a) Joints with irregular triangular asperities, on which asperities are of different dip angles (10°, 20° and 30°); (b) joints with regular triangular asperities, on which the dip angle of asperities equals to 30°; and (c) planar joints with no asperities.

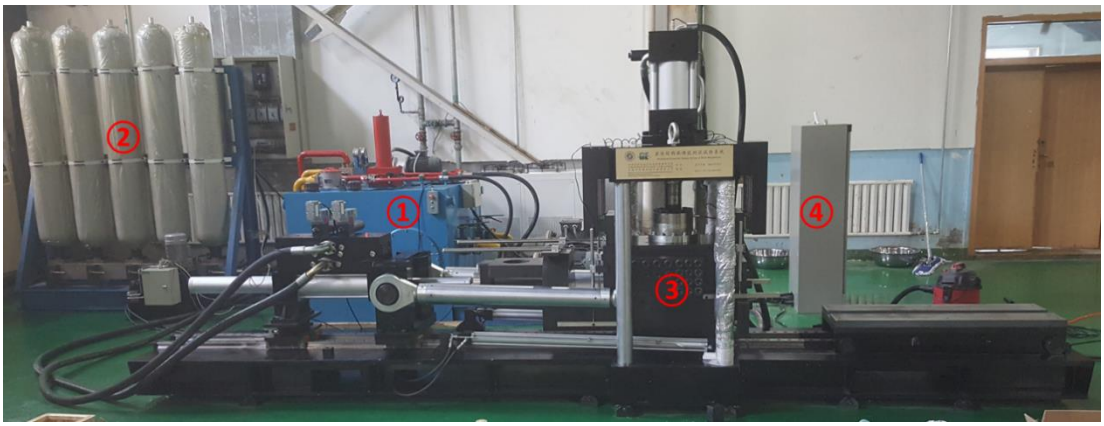

Fig. 2 The dynamic direct shear testing system, which consists of four components: ① Hydraulic aggregate, ② air pressure accumulators, ③ shear box with horizontal and vertical frames, and ④ electronic control unit.

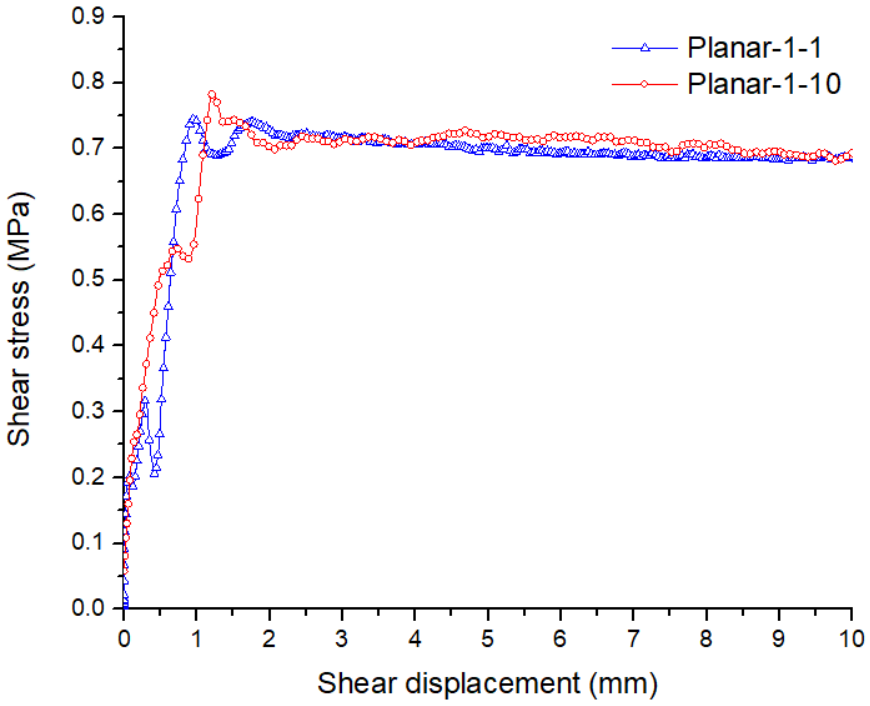
Planar-1-1
Planar-1-10
Shear stress (MPa)
Shear displacement (mm)
0.0
0.1
0.2
0.3
0.4
0.5
0.6
0.7
0.8
0.9
0
1
2
3
4
5
6
7
8
9
10

(a)

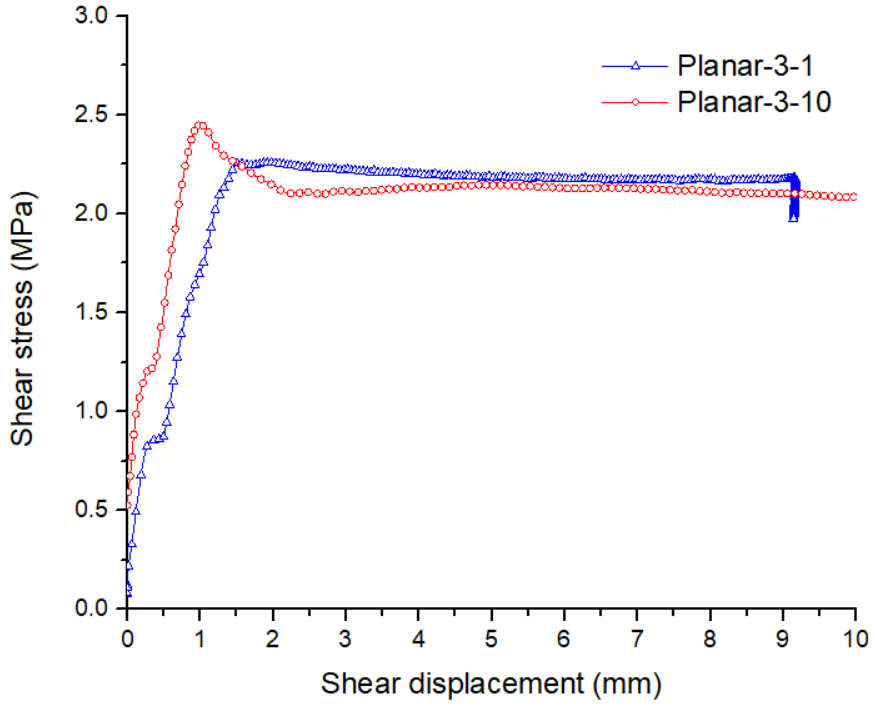
Planar-3-1
Planar-3-10
Shear stress (MPa)
Shear displacement (mm)
0.0
0.5
1.0
1.5
2.0
2.5
3.0
0
1
2
3
4
5
6
7
8
9
10

(b)

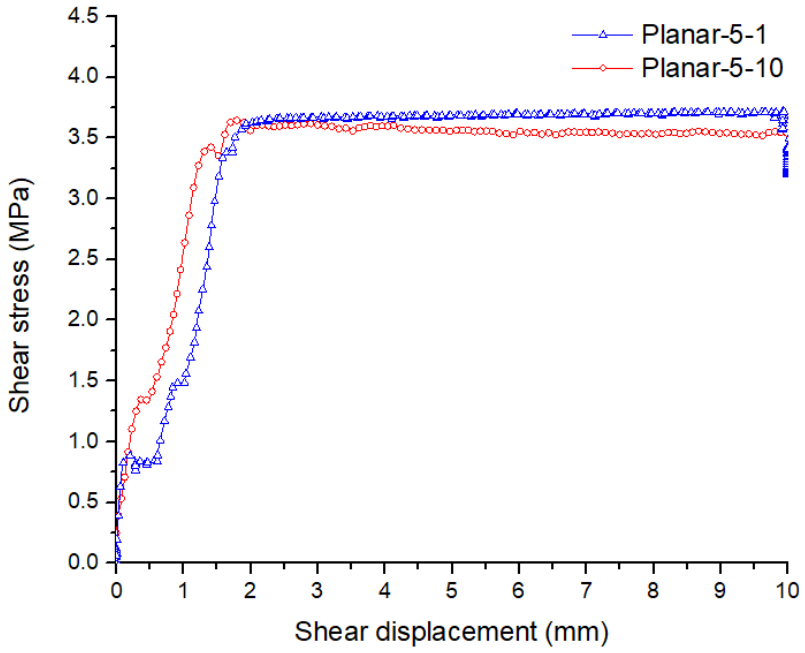

(c)

Fig. 3 The shear stress-shear displacement responses of unpolished planar joints at shear rates of 1 mm/s and 10 mm/s under the normal stress of: (a) 1 MPa; (b) 3 MPa; and (c) 5 MPa. Samples are labeled following "Joint type-normal stress (unit: MPa)-shear rate (unit: mm/s)".

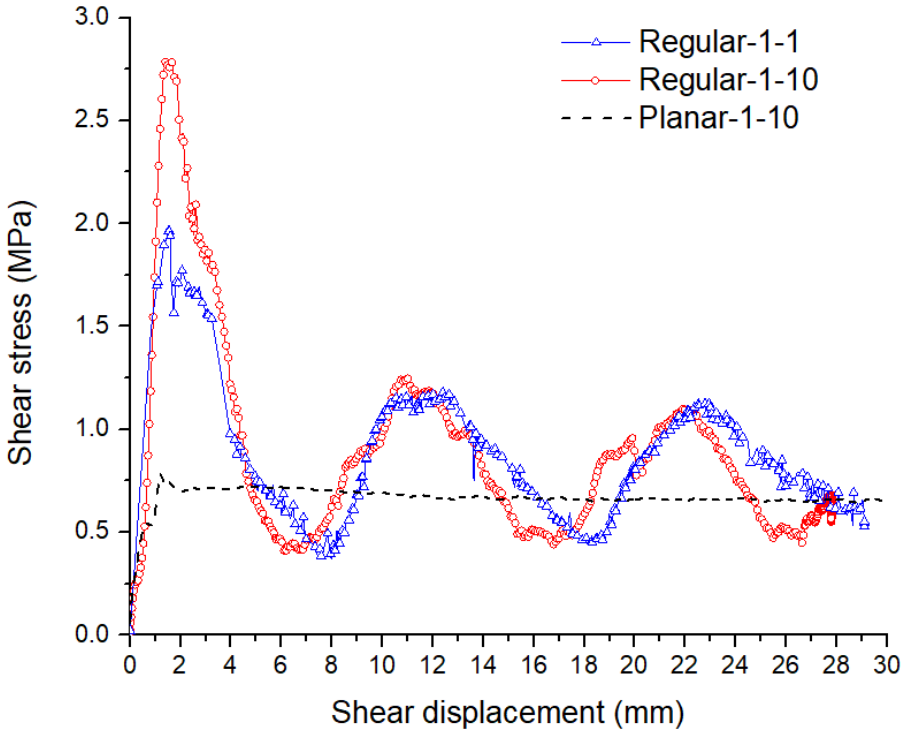
Regular-1-1
Regular-1-10
Planar-1-10
Shear stress (MPa)
Shear displacement (mm)
0.0
0.5
1.0
1.5
2.0
2.5
3.0
0
2
4
6
8
10
12
14
16
18
20
22
24
26
28
30

(a)

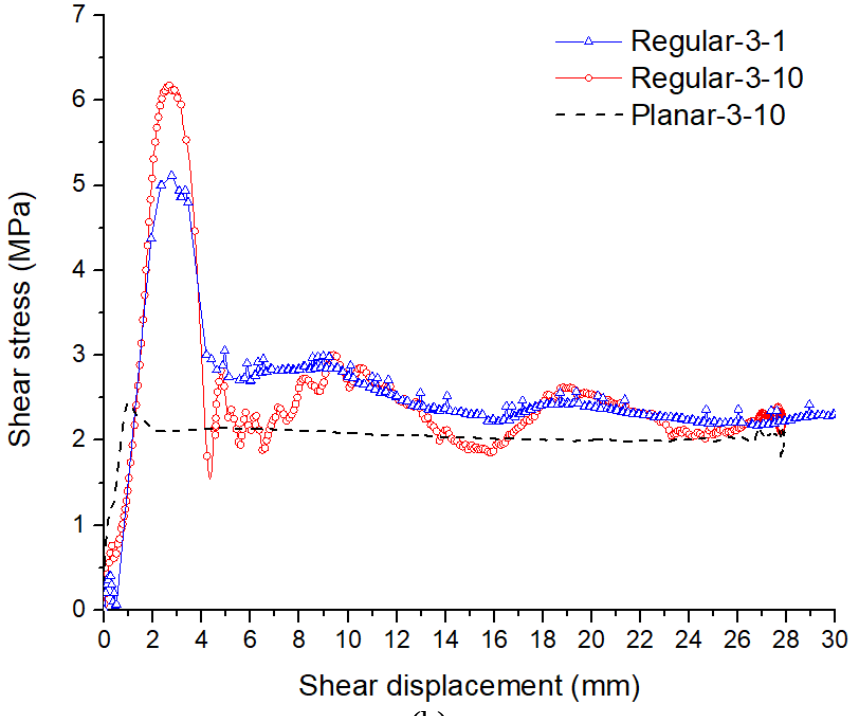
Regular-3-1
Regular-3-10
Planar-3-10
Shear stress (MPa)
Shear displacement (mm)
0
1
2
3
4
5
6
7
0
2
4
6
8
10
12
14
16
18
20
22
24
26
28
30

(b)

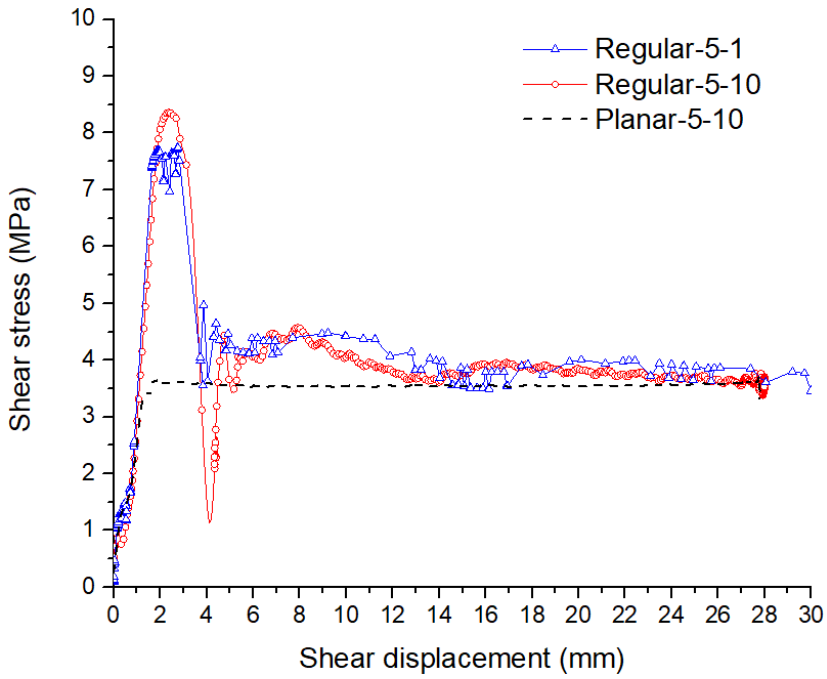

(c)

Fig. 4 Shear stress-shear displacement responses of the joints with regular asperities at shear rates of 1 mm/s and 10 mm/s under the normal stresses of: (a) 1 MPa; (b) 3 MPa; and (c) 5 MPa. Samples are labeled following "Joint type-normal stress (unit: MPa)-shear rate (unit: mm/s)".

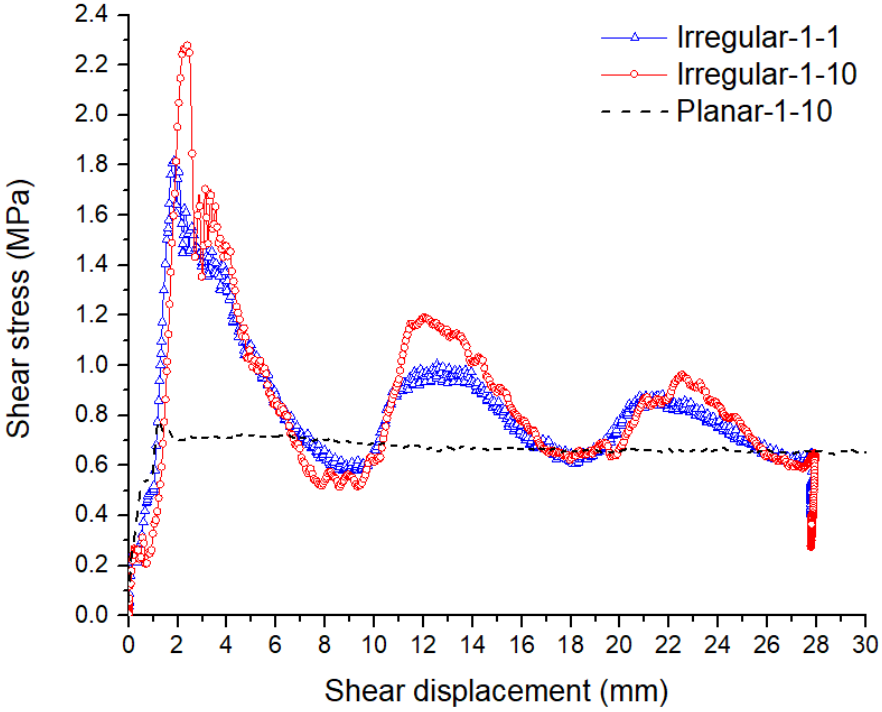
Irregular-1-1
Irregular-1-10
Planar-1-10
Shear stress (MPa)
Shear displacement (mm)
0.0
0.2
0.4
0.6
0.8
1.0
1.2
1.4
1.6
1.8
2.0
2.2
2.4
0
2
4
6
8
10
12
14
16
18
20
22
24
26
28
30

(a)

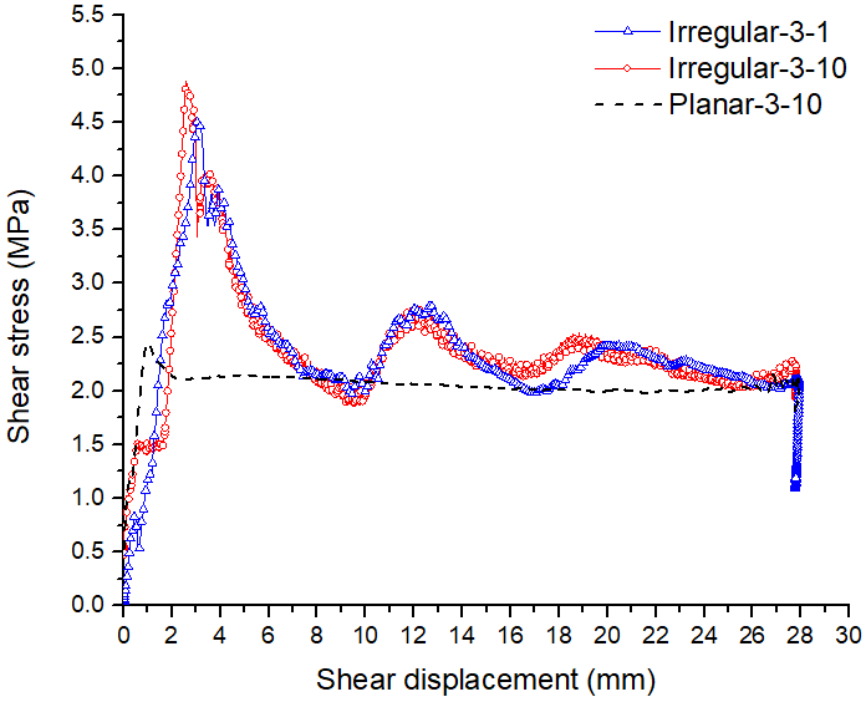
Irregular-3-1
Irregular-3-10
Planar-3-10
Shear stress (MPa)
Shear displacement (mm)
0.0
0.5
1.0
1.5
2.0
2.5
3.0
3.5
4.0
4.5
5.0
5.5
0
2
4
6
8
10
12
14
16
18
20
22
24
26
28
30

(b)

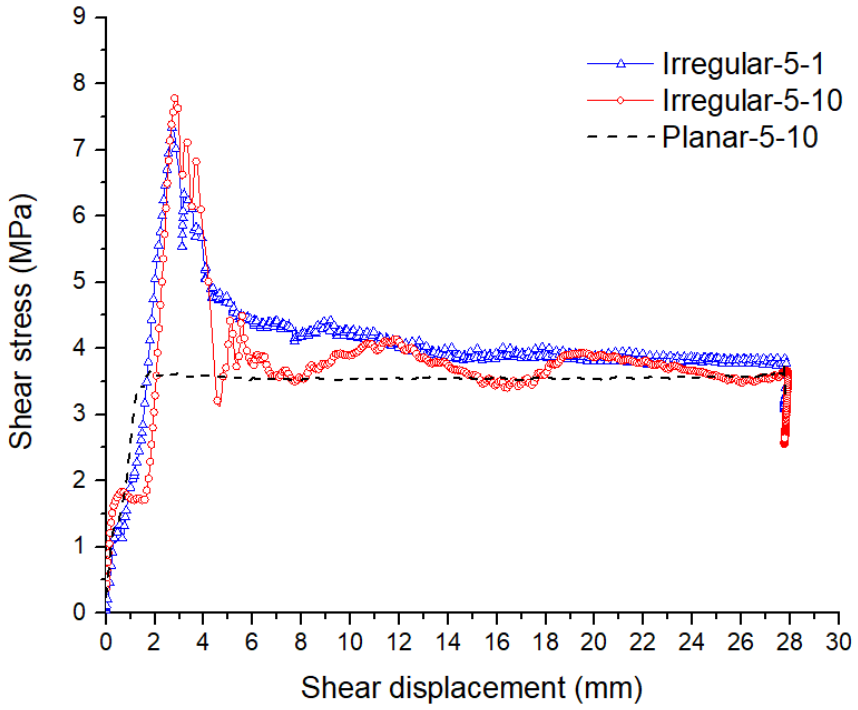

(c)

Fig. 5 The shear stress-shear displacement responses of joints with irregular asperities at shear rates of 1 mm/s and 10 mm/s under the normal stress of: (a) 1 MPa; (b) 3 MPa; and (c) 5 MPa. Samples are labeled following "Joint type-normal stress (unit: MPa)-shear rate (unit: mm/s)".

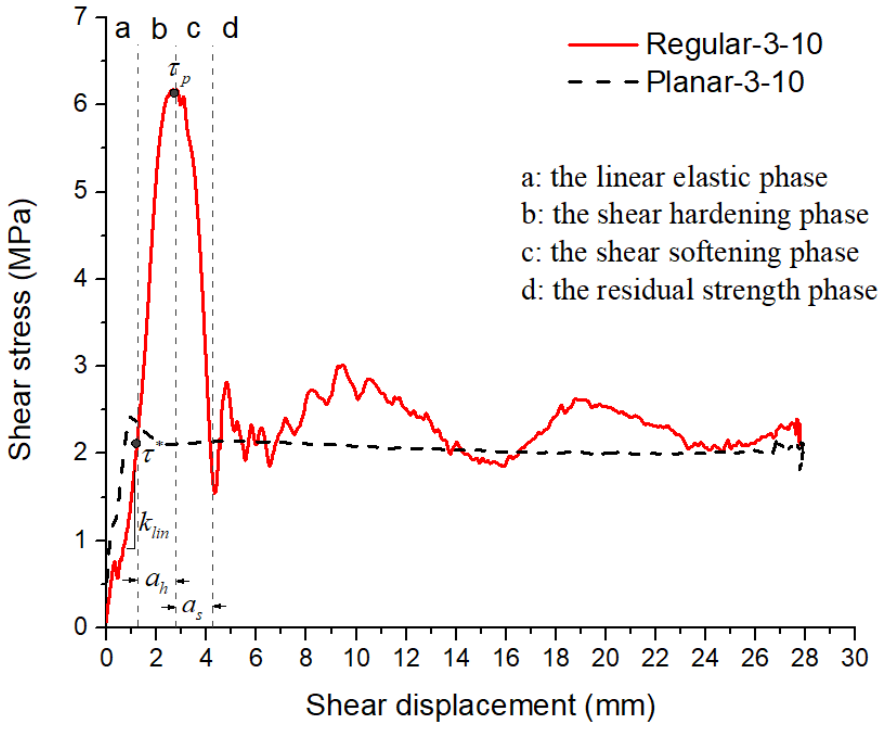

Fig. 6 Four phases of the shear stress-shear displacement curve of rough joints (taking the Sample "Regular-3-10" as an example): the linear elastic phase, the shear hardening phase, the shear softening phase, and the residual strength phase. Here, a_h and a_s denote the projected length of the curve in the hardening and softening phases, respectively, k_{lin} is the linear stiffness, τ^* is the initial yield limit, and τ_p is the peak strength, a_h is the total shear displacement in hardening phase, a_s is the total shear displacement in softening phase.

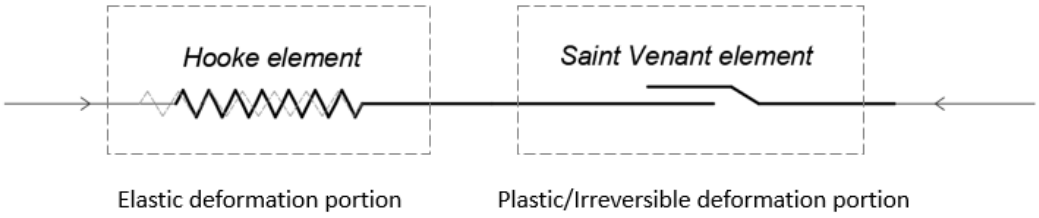

Fig. 7 Sketch of the Hooke-Saint Venant model

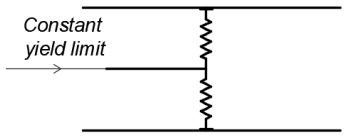

(a)

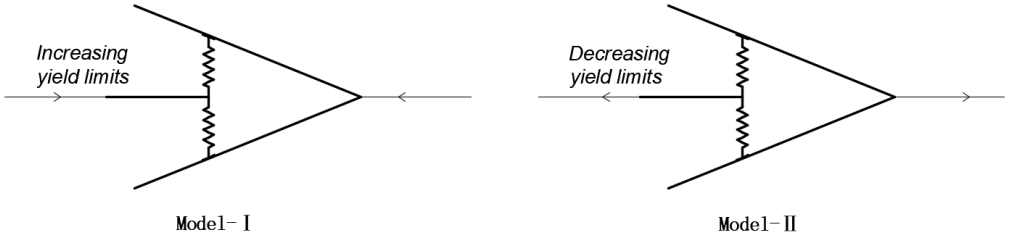

(b)

Fig. 8 Sketches of the (a) traditional and (b) modified Saint Venant elements. Due to the inclining frictional surfaces, yield strength increases under loading conditions (Model-I) and decreases under unloading conditions (Model-II).

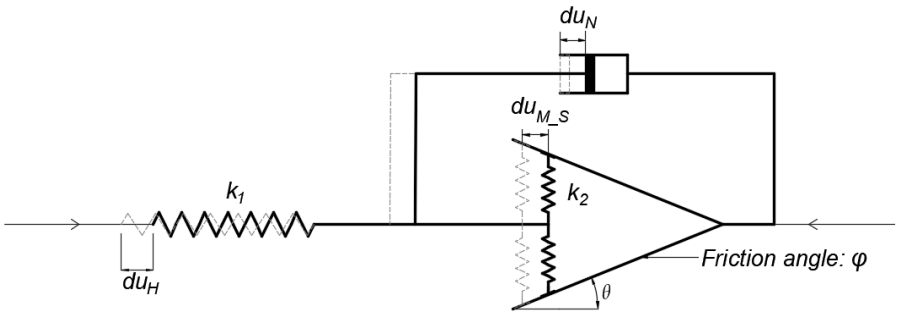

(a)

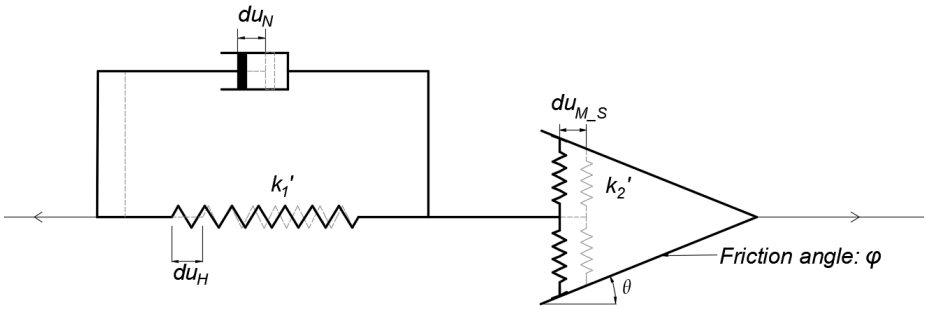

(b)

Fig. 9 Sketches of (a) the Hooke-modified Saint Venant/Newton model and (b) the Hooke/Newton-modified Saint Venant model. k_1, k_2, k_1' and k_2' are the spring stiffness; du_H, du_{M_S} and du_N are displacement increments of Hooke, modified Saint Venant and Newton elements, respectively; θ and φ are the dip angle and fictional angle of the frictional surfaces in the modified Saint Venant element, respectively.

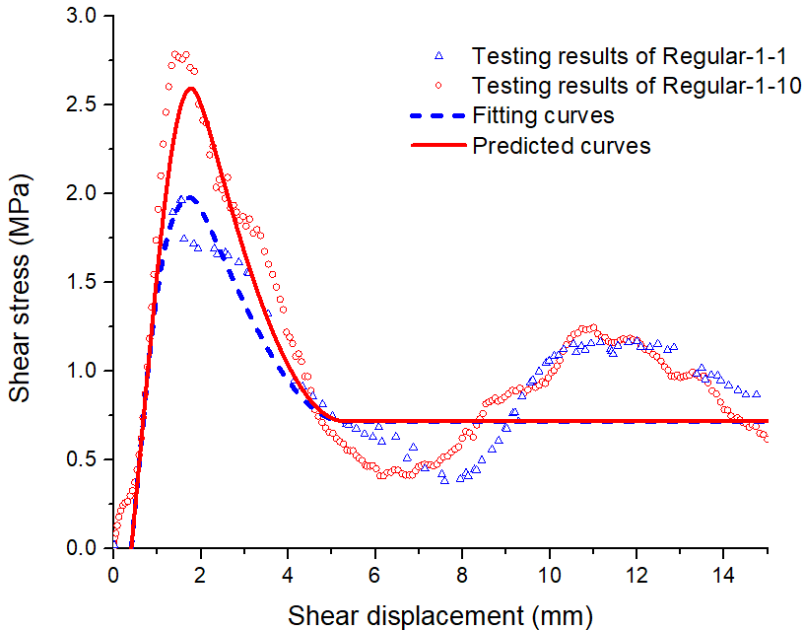
Testing results of Regular-1-1
Testing results of Regular-1-10
Fitting curves
Predicted curves
Shear stress (MPa)
Shear displacement (mm)
0.0
0.5
1.0
1.5
2.0
2.5
3.0
0
2
4
6
8
10
12
14

(a)

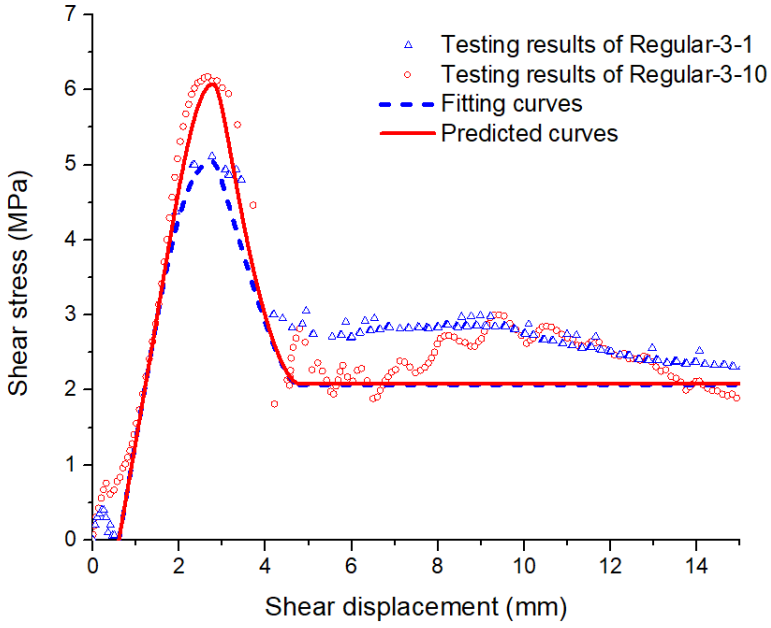
Testing results of Regular-3-1
Testing results of Regular-3-10
Fitting curves
Predicted curves
Shear stress (MPa)
Shear displacement (mm)
0
1
2
3
4
5
6
7
0
2
4
6
8
10
12
14

(b)

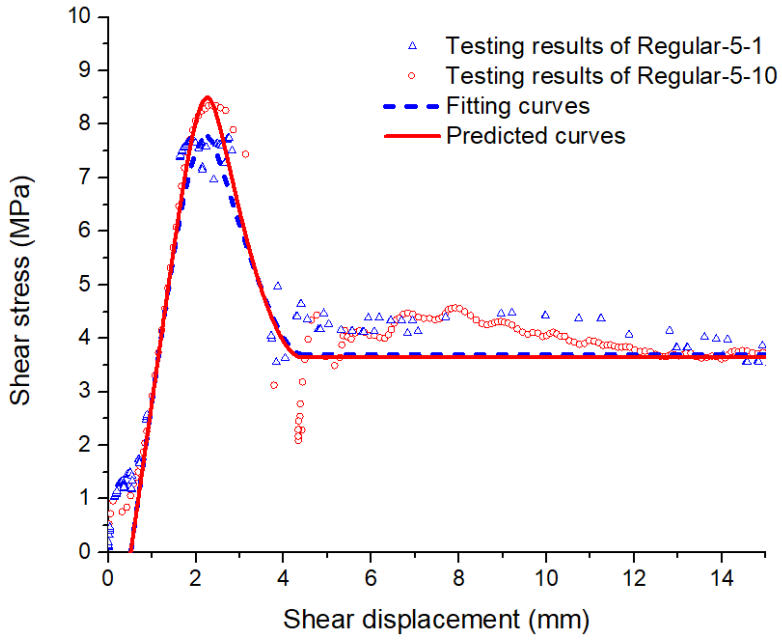

(c)

Fig.10 Shear stress-shear displacement curves of joints with regular asperities obtained from laboratory tests and the proposed joint model at shear rates of 1 mm/s and 10 mm/s, where the normal stress applied was: (a) 1 MPa; (b) 3 MPa; and (c) 5 MPa. The predicted curves were obtained on the basis of the fitting curves.

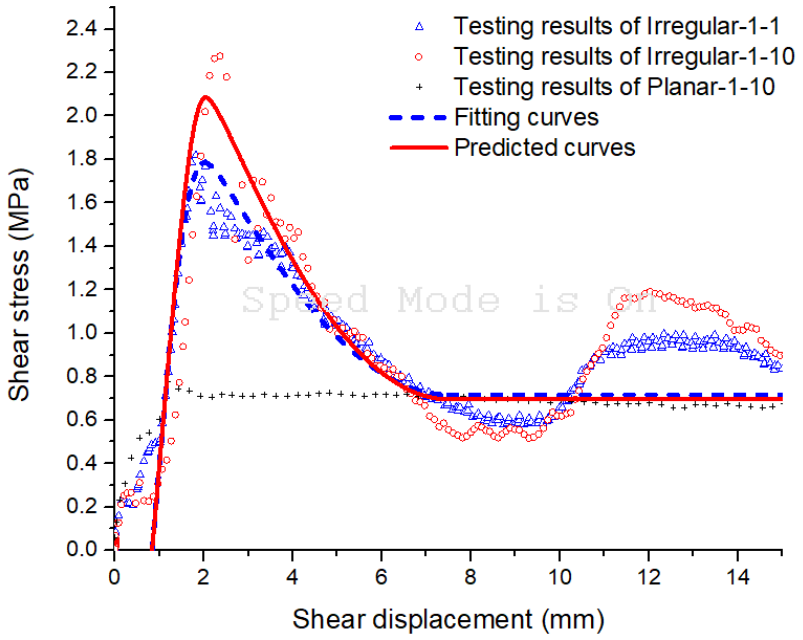
Testing results of Irregular-1-1
Testing results of Irregular-1-10
Testing results of Planar-1-10
Fitting curves
Predicted curves
Shear stress (MPa)
Shear displacement (mm)
0.0
0.2
0.4
0.6
0.8
1.0
1.2
1.4
1.6
1.8
2.0
2.2
2.4
0
2
4
6
8
10
12
14

(a)

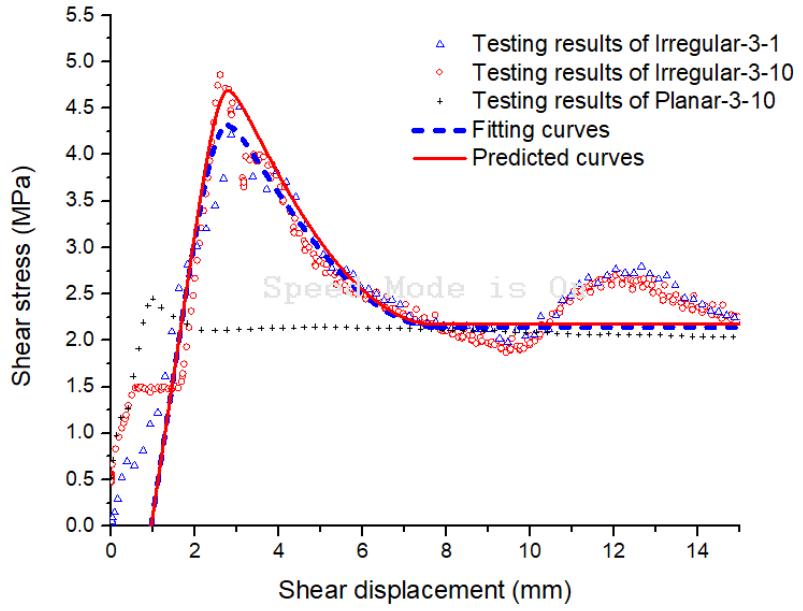
Testing results of Irregular-3-1
Testing results of Irregular-3-10
Testing results of Planar-3-10
Fitting curves
Predicted curves
Shear stress (MPa)
Shear displacement (mm)
0.0
0.5
1.0
1.5
2.0
2.5
3.0
3.5
4.0
4.5
5.0
5.5
0
2
4
6
8
10
12
14

(b)

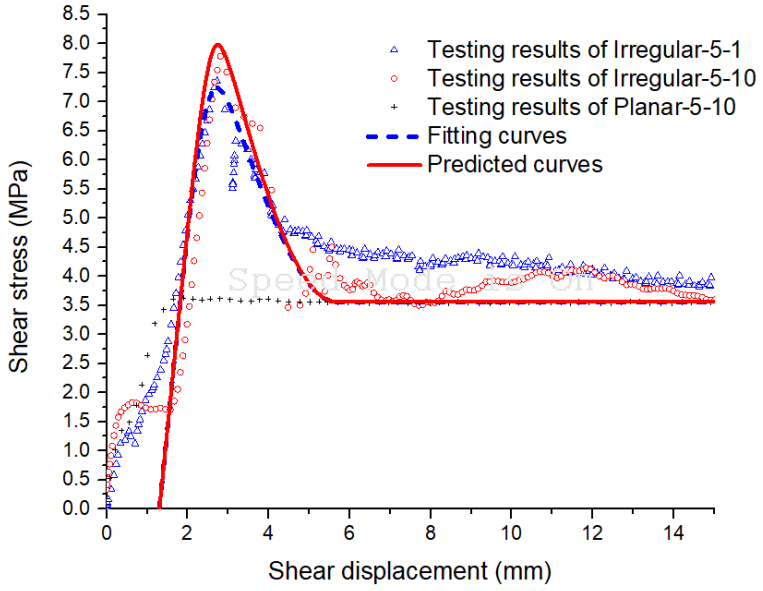

(c)

Fig.11 Shear stress-shear displacement curves of joints with irregular asperities obtained from laboratory tests and the proposed joint model, where the normal stress applied was: (a) 1 MPa; (b) 3 MPa; and (c) 5 MPa. The predicted curves were obtained on the basis of the fitting curves. The kinetic frictional strength of planar joints was added here to make a comparison with the residual strength of joints with irregular asperities.

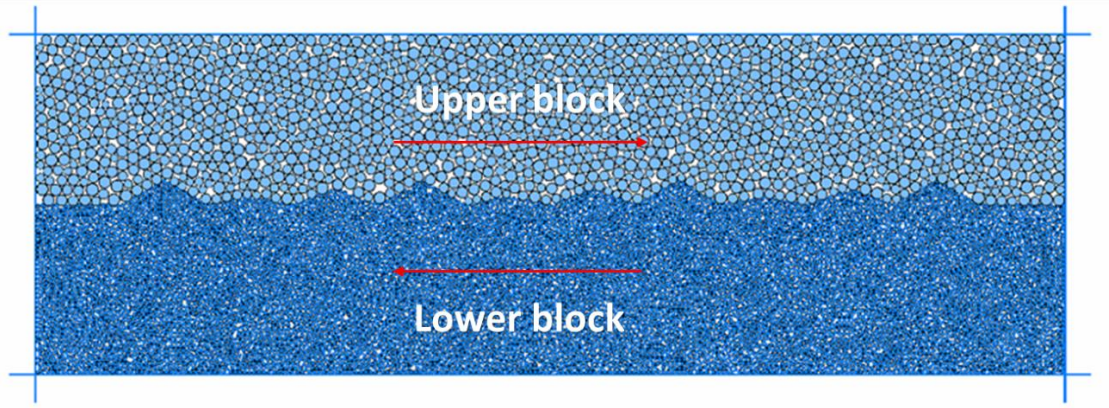

Fig. 12 The geometric model of the joint with irregular asperities used in the numerical shear test. Particles in the upper and lower blocks were generated with different size ranges to alleviate the periodic fluctuation in contact number during shearing.

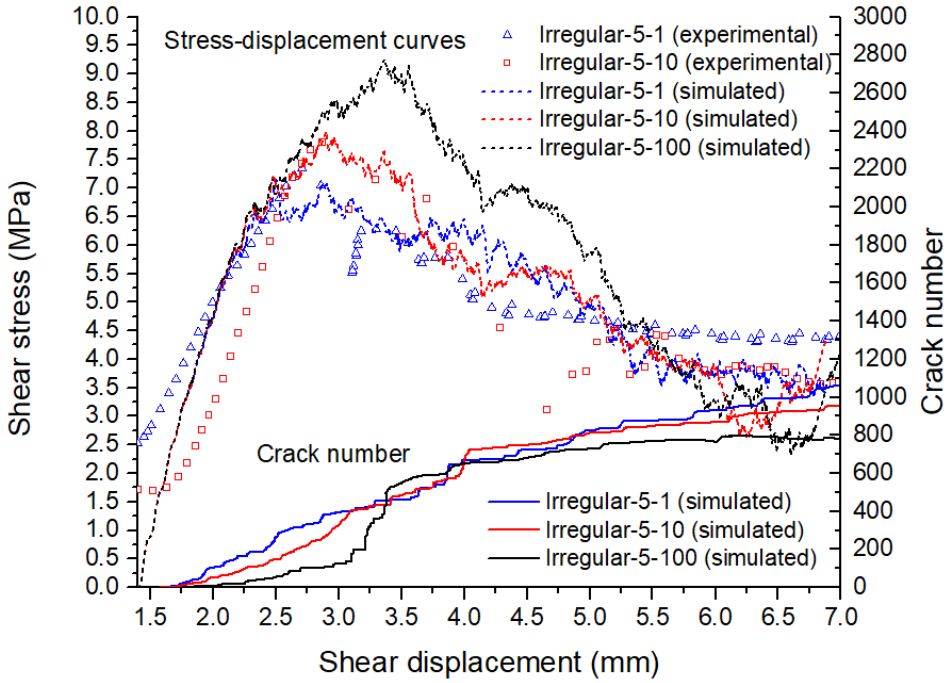

Fig. 13 The evolution of shear stress and crack number as a function of shear displacement from the numerical and laboratory direct shear tests of joints with irregular asperities, where the normal stresses applied were 5 MPa. The shear rates applied in the laboratory tests were 1 mm/s and 10 mm/s, while the shear rates applied in the numerical simulations were 1mm/s, 10 mm/s and 100 mm/s. To eliminate the influence of the gap between the joint sample and the shear box, the horizontal coordinate starts from 1.4 mm.

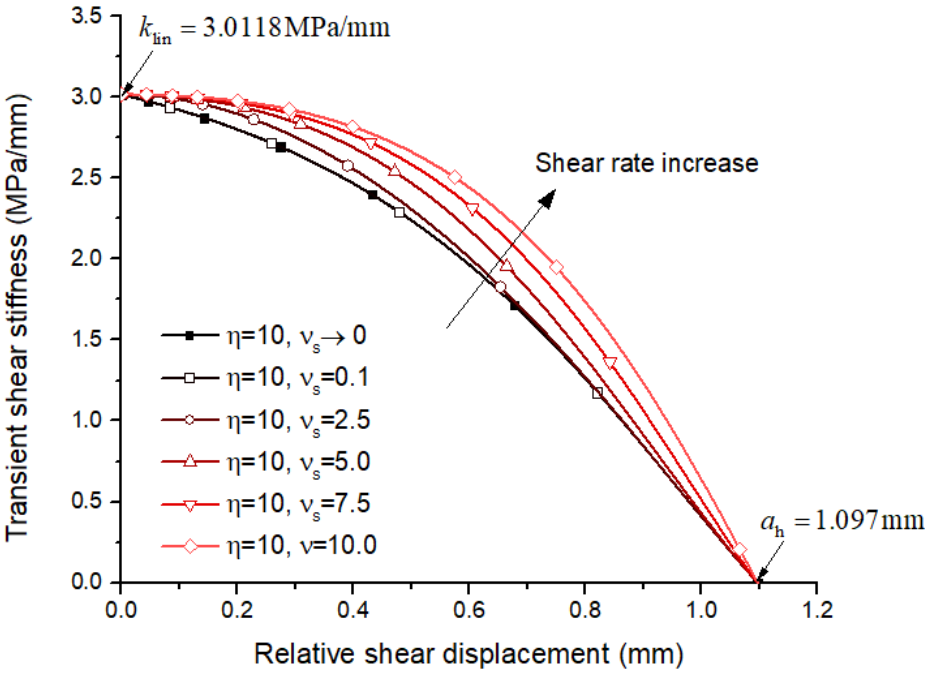

(a)

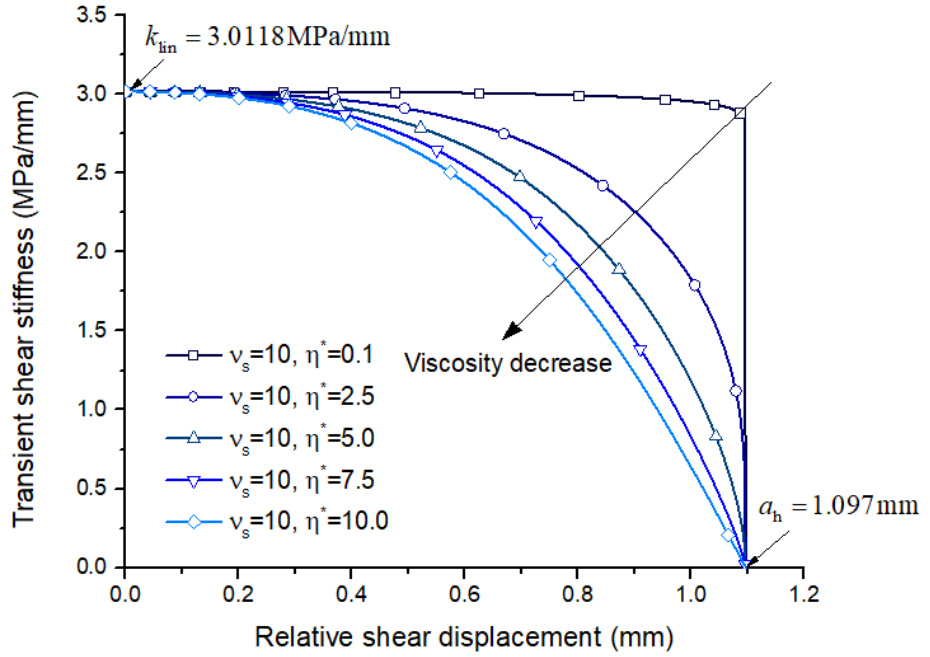

(b)

Fig. 14 The shear stiffness-shear displacement relation in the hardening phase calculated by Eqs. (20) and (22) with different: (a) v_s, and (b) different η^*. The values of model parameters are from testing results of the Sample Irregular-3-1/Irregular-3-10.

Table 1 Values of parameters used in the proposed model for regular joints

Sample	Phase	k_{lin} (MPa/mm)	k_2 or k_2' (MPa/mm)	a_h or a_s (mm)
Regular-1-1/ Regular -1-10	hardening	2.6447	0.5	1.1
	softening	-2.6447	-0.6	3.5
Regular -3-1/ Regular -3-10	hardening	3.356	1.1	1.54
	softening	-3.356	-5.7	2.01
Regular -5-1/ Regular -5-10	hardening	5.7913	4.3	1.133
	softening	-5.7913	-5.59	2.16

Note: The viscosity-related material constant $\eta^*$is equal to 10 mm/s

Table 2 Values of parameters used in the proposed model for irregular joints

Sample	Phase	k_{lin} (MPa/mm)	k_2 or k_2' (MPa/mm)	a_h or a_s (mm)
Irregular-1-1/ Irregular -1-10	hardening	2.3663	0.85	0.9
	softening	-2.3663	-0.265	5.46
Irregular -3-1/ Irregular -3-10	hardening	3.0188	2.2	1.097
	softening	-3.0188	-0.66	4.975
Irregular -5-1/ Irregular -5-10	hardening	6.9129	3.9	0.9127
	softening	-6.9129	-2.51	2.926

Note: The viscosity-related material constant $\eta^*$is equal to 10 mm/s

Table 3 The values of the micro-parameters used for the parallel bond model (PBM) and smooth joint contact model (SJM) in PFC

PBM parameters	*The upper block*	*The lower block*
Particle radius range (mm)	0.5-0.8	0.25-0.3
Effective modulus (GPa)	5.9	5.2
$\mathbf{k_n/k_s}$	1.57	1.4
Frictional coefficient	0.6	0.6
Normal strength (MPa)	23	21.8
Shear strength (MPa)	23	21.8
SJM parameters		
Normal stiffness (GPa/m)	21.6	
Shear stiffness (GPa/m)	8.9	
Frictional coefficient	0.7	